Quasi-Relativistic Calculation of EPR g-Tensors with Derivatives of the Decoupling Transformation, Gauge-Including Atomic Orbitals, and Magnetic Balance

Yannick J. Franzke[*,†] and Jason M. Yu[*,‡]

†Fachbereich Chemie, Philipps–Universität Marburg, 35032 Marburg, Germany

‡Department of Chemistry, University of California, Irvine, 1102 Natural Sciences II, Irvine, CA 92697-2025, USA

E-mail: yannick.franzke@chemie.uni-marburg.de; yujm1@uci.edu

Abstract

We present an exact two-component (X2C) ansatz for the EPR g-tensor using gauge-including atomic orbitals (GIAOs) and a magnetically balanced basis set expansion. In contrast to previous X2C and "fully" relativistic ansätze for the g-tensor, this implementation results in a gauge-origin invariant formalism. Furthermore, the derivatives of the relativistic decoupling matrix are considered to form the complete analytical derivative of the X2C Hamiltonian. To reduce the associated computational costs, we apply the diagonal local approximation to the unitary decoupling transformation (DLU) and the (multipole-accelerated) resolution of the identity approximation. The X2C ansatz is compared to Douglas–Kroll–Hess theory and the zeroth-order regular approximation for 11 diatomic molecules. The impact of the relativistic Hamiltonian, the basis set, and the density functional approximation is subsequently assessed for

1

a set of 17 transition-metal complexes to complement our previous work on the hyperfine coupling constant [DOI: 10.33774/chemrxiv-2021-wnz1v-v2]. In total, 24 basis sets and 22 density functional approximations are considered. The quasi-relativistic X2C and DLU-X2C Hamiltonians accurately reproduce the results of the parent "fully" relativistic four-component theory when accounting for two-electron picture-change effects with the modified screened nuclear spin–orbit approximation in the respective one-electron integrals and integral derivatives. Generally, the uncontracted Dyall and segmented-contracted Karlsruhe x2c-type basis sets perform well when compared to large even-tempered basis sets. Moreover, (range-separated) hybrid density functional approximations are needed to match the experimental findings. Here, hybrids based on the *meta*-generalized gradient approximation are not an *a priori* improvement. Compared to the other computational parameters, the impact of the GIAOs and the magnetic balance on the actual results in standard calculations is less pronounced. Routine calculations of large molecules are possible with widely available and comparably low-cost hardware as demonstrated for $[Pt(C_6Cl_5)_4]^-$ with 3360 basis functions and three spin-(1/2) La(II) and Lu(II) compounds. Both approaches based on a common gauge origin and GIAOs using triple-ζ basis sets lead to a good agreement with the experimental findings. The best agreement is found with hybrid functionals such as PBE0 and ωB97X-D.

1   Introduction

Electron paramagnetic resonance (EPR) spectroscopy is an essential experimental tool for the study of open-shell systems, especially for transition-metal and lanthanide compounds. The EPR spectrum consists of two important parameters—namely, the g-tensor used to indicate the shift relative to the free electron g-factor and the hyperfine coupling (HFC) constant. An understanding of the spectrum often requires quantum chemical studies to interpret the experimental findings.[1–7] For example, predictions of EPR parameters from

theory have helped to investigate the electronic origin of hyperfine clock transitions,[8] as well as validate trends in magnetic anisotropy orientations,[9] for distinct classes of lanthanide single molecule magnets (SMMs), to name only a few recent applications. These parameters can be compared directly to those extracted from experimental spectra, which is carried out through fitting the data to an effective spin Hamiltonian.[1]

From a theoretical point of view, the g-tensor is an intrinsic relativistic property, and spin–orbit coupling is of the utmost importance for accurate calculations. Keystone methods used in relativistic quantum chemistry[10–19] include the application of the zeroth-order regular approximation[20–22] (ZORA) to the g-tensor,[23–26] the two-component (2c) Douglas–Kroll–Hess (DKH) ansatz by Malkin *et al.*,[27] and the "fully" relativistic four-component (4c) Dirac–Kohn–Sham theory by Komorovsky and co-workers.[28–31] The latter is undoubtedly the most accurate relativistic treatment. However, it also leads to considerable computational costs compared to the quasi-relativistic two-component ansätze. Today, both ZORA and DKH, as well as other approximate quasi-relativistic Hamiltonians, are replaced by (one-electron) exact two-component (X2C) theory[32–38] in many quantum chemistry program suites.[39–48] The application of analytical derivative theory[49,50] to X2C is rather straightforward compared to the more involved formulation in DKH.[51,52] Complete analytical derivatives of the X2C Hamiltonian are available for geometry derivatives,[53–59] electric properties,[60–63] and various magnetic properties.[64–74]

The application of X2C to EPR parameters was pioneered in the groups of Autschbach[75,76] and Kaupp.[77] These works neglect the derivatives of the relativistic decoupling transformation, which may be motivated by reduced computational costs and the minor impact on the HFC constant.[72,73] Yet, their importance is still to be determined explicitly for the g-tensor. Moreover, the restricted kinetic balance (RKB) condition[78] and a common gauge origin (CGO) are employed for the g-tensor in Ref. 77. From a formal point of view, the RKB condition needs to be generalized to the restricted magnetic balance (RMB) condition,[79] i.e. the vector potential needs to be included in the basis set expansion of the small compo-

nent. This ensures the exact non-relativistic limit of the Dirac equation in the presence of an external magnetic field and the errors in the orbital energies are on the order of $\mathcal{O}(c^{-4})$ with finite basis sets.[79] The use of RMB leads to problematic integrals for the HFC constant and the related nuclear magnetic resonance (NMR) coupling constants in X2C.[69] Moreover, the impact was found to be of minor importance for derivatives with respect to the nuclear magnetic moments.[69,71] However, the integrals can be evaluated straightforwardly for magnetic field derivatives.[66–68,70] Thus, the RMB can be used for EPR g-tensors similar to NMR shielding constants[66–68,70] and magnetic circular dichroism.[80]

As mentioned previously, a common gauge origin is used in both X2C[77] and 4c[28–31] calculations of the g-tensor so far. Formally, the g-tensor depends on the chosen gauge origin in finite basis set calculations.[81] Consequently, the so-called gauge-including atomic orbitals[82,83] (GIAOs) are employed to remove the gauge-origin dependence. This issue is of great importance for NMR shieldings and GIAOs are thus routinely included in their relativistic calculation.[66–68,70,84–91] In contrast to NMR shieldings, the g-tensor is a global property of the full molecule and the gauge dependence is less pronounced.[92,93] However, GIAOs are still commonly employed in non-relativistic calculations[93–98] and their use in relativistic calculations is also desirable. For instance, a two-component gauge-origin invariant ZORA ansatz was implemented by Verma and Autschbach.[26]

Therefore, we extend the available X2C framework for EPR g-tensors in four aspects. First, the derivatives of the unitary decoupling transformation are included to arrive at the complete derivative of the X2C Hamiltonian. Second, the magnetic balance condition[79] is employed. Third, gauge-including atomic orbitals[82,83] are used for the basis set expansion. Fourth, the diagonal local approximation to the unitary decoupling transformation[99] (DLU) is introduced for g-tensors, as solving the one-electron X2C response equations for the decoupling derivatives becomes demanding for large molecules, and local approximations are therefore desirable[100–103] to perform routine calculations of large molecules and metal clusters.[104–107]

2 Theory

2.1 Notation

We use the same notation as in our work on the HFC constant.[73] L and S refer to the large and small component, respectively. The subscripts $+$ and $-$ indicate the states of the negative- and positive-energy subspace, which are commonly called positronic and electronic states. $\mathbb{M}$ denotes a matrix in the 4c space, while matrices in the space of spin-free one-component (1c) basis functions $\{\lambda_\mu\}$ are indicated as $\mathbf{M}$ and matrices in the 2c space ($\{\phi_\mu\}$ = $\{\lambda_\mu\} \otimes \{\alpha, \beta\}$) are indicated as $\boldsymbol{M}$. Cartesian coordinates are denoted with the subscripts u, v while the superscript B indicates derivatives that are formed according to

$$\boldsymbol{h}_u^B = \left(\frac{\mathrm{d}\boldsymbol{h}}{\mathrm{d}B_u}\right)_{B_u=0} \tag{1}$$

We use Gaussian-based atomic units throughout this work.

2.2 Definition of the EPR g-Tensor

We use the approach of Malkin *et al.* for the relativistic g-tensor[27,28]

$$g_{uv} = \frac{\mathrm{d}^2E}{\mathrm{d}B_u\mathrm{d}S_v}\bigg|_{\vec{B}=0} = \frac{2c}{\langle\tilde{S}_v\rangle}\frac{\mathrm{d}E(J_v, \vec{B})}{\mathrm{d}B_u}\bigg|_{\vec{B}=0} \tag{2}$$

with the external magnetic field $\vec{B}$ and the effective spin $\vec{\tilde{S}}$. The energy is calculated with the non-collinear approach,[108] where the magnetization vector $\vec{J}$ and the spin $\vec{S}$ are aligned along three orthogonal axes v. The effective spin is determined by the configuration of the electronic ground state, and converged orbitals of a 1c calculation are needed to ensure a good starting point. We note in passing that Verma and Autschbach used a generalized collinear ansatz with a chosen spin quantization for the EPR g-tensor[26] and the HFC tensor[109] in a ZORA framework.

2.3   X2C Hamiltonian in the Presence of a Magnetic Field

Magnetic perturbations are introduced into the Dirac equation with the principle of minimal coupling or minimal substitution.[110] The linear momentum operator $\hat{\vec{p}}$ is generalized to $\hat{\vec{\pi}}$ according to

$$\hat{\vec{p}} \longrightarrow \hat{\vec{\pi}} = \hat{\vec{p}} + \frac{1}{c}\hat{\vec{\mathcal{A}}} \tag{3}$$

where $\hat{\vec{\mathcal{A}}}$ denotes the vector potential. For g-tensors, the vector potential of a static and homogeneous external magnetic field reads

$$\vec{\mathcal{A}}_O(\vec{r}) = \frac{1}{2}\vec{B} \times \vec{r}_O \tag{4}$$

$$\vec{r}_O = \vec{r} - \vec{R}_O \tag{5}$$

$\vec{R}_O$ refers to the gauge origin, which bears no physical meaning and the obtained molecular properties should be gauge-origin independent. Therefore, explicit field-dependent basis functions, the so-called gauge-including atomic orbitals or London orbitals, are introduced[82,83]

$$\lambda_\mu\left(\vec{B}, \vec{r}\right) = \exp\left(-\mathrm{i}\Lambda_{\mu O}\right)\lambda_\mu\left(\vec{r}\right) \tag{6}$$

$$\Lambda_{\mu O}\left(\vec{B}, \vec{r}\right) = \frac{1}{2c}(\vec{R}_{\mu O} \times \vec{r}) \cdot \vec{B} \tag{7}$$

Here, a (real) field-independent basis function λ_μ is augmented by a complex phase prefactor. We use the notation $\vec{R}_{\mu O} = \vec{R}_\mu - \vec{R}_O$, where $\vec{R}_\mu$ denotes the atom center of the respective basis function. Note that we use the Coulomb gauge in this work.

The one-electron Dirac–Hamilton operator in the presence of an external magnetic field reads

$$\hat{h}_{\mathrm{D}} = c\vec{\alpha} \cdot \hat{\vec{\pi}} + (\beta - I_4)\,c^2 + \hat{V} \tag{8}$$

6

Here, α and β are trace-less quantities defined as

$$\alpha_i = \begin{pmatrix} 0_2 & \sigma_i \\ \sigma_i & 0_2 \end{pmatrix}, \qquad \beta = \begin{pmatrix} \sigma_0 & 0_2 \\ 0_2 & -\sigma_0 \end{pmatrix}, \tag{9}$$

$\vec{\sigma} = (\sigma_x, \sigma_y, \sigma_z)$, is a vector consisting of the Pauli spin matrices

$$\sigma_x = \begin{pmatrix} 0 & 1 \\ 1 & 0 \end{pmatrix}, \qquad \sigma_y = \begin{pmatrix} 0 & -i \\ i & 0 \end{pmatrix}, \qquad \sigma_z = \begin{pmatrix} 1 & 0 \\ 0 & -1 \end{pmatrix} \tag{10}$$

while σ_0 denotes the (2×2) identity matrix. $\hat{V}$ is the electron-nucleus potential and I_4 is the (4×4) unit matrix. The basis set expansion using the restricted magnetic balance condition reads[79]

$$\left| \psi_i^L \right\rangle = \sum_\mu C_{\mu i}^L e^{-i\Lambda_\mu O} \left| \phi_\mu \right\rangle \tag{11}$$

$$\left| \psi_i^S \right\rangle = \sum_\mu C_{\mu i}^S e^{-i\Lambda_\mu O} \frac{1}{2c} \vec{\sigma} \cdot \left(\hat{\vec{p}} + \frac{1}{c} \hat{\vec{\mathcal{A}}}_\mu \right) \left| \phi_\mu \right\rangle \tag{12}$$

where we used the identities of Ref. 79 to move the GIAO prefactor to the left of the generalized momentum in Eq. 12. This basis set expansion results in the Dirac equation in a matrix representation according to[66–68,70]

$$\mathbb{DC} = \mathbb{MCE} \tag{13}$$

In the super-matrix form, this reads

$$\begin{pmatrix} V & \Pi^\dagger \\ \Pi & (\frac{1}{4c^2} W - T) \end{pmatrix} \begin{pmatrix} C_-^L & C_+^L \\ C_-^S & C_+^S \end{pmatrix} = \begin{pmatrix} S & 0_2 \\ 0_2 & \frac{1}{2c^2} T \end{pmatrix} \begin{pmatrix} C_-^L & C_+^L \\ C_-^S & C_+^S \end{pmatrix} \begin{pmatrix} \epsilon_- & 0_2 \\ 0_2 & \epsilon_+ \end{pmatrix} \tag{14}$$

The overlap matrix S and the potential matrix V are well known from non-relativistic

quantum chemistry. These matrices are block-diagonal in the (2×2) superspace and are given by

$$
\boldsymbol{S} = \begin{pmatrix} \mathbf{S} & 0 \\ 0 & \mathbf{S} \end{pmatrix}, \mathbf{S}_{\mu\nu} = \langle \lambda_\mu | e^{i\Lambda_{\mu\nu}} | \lambda_\nu \rangle \tag{15}
$$

$$
\boldsymbol{V} = \begin{pmatrix} \mathbf{V} & 0 \\ 0 & \mathbf{V} \end{pmatrix}, \mathbf{V}_{\mu\nu} = \langle \lambda_\mu | e^{i\Lambda_{\mu\nu}} \hat{V} | \lambda_\nu \rangle \tag{16}
$$

All other matrices are not block-diagonal anymore and read

$$
\boldsymbol{\Pi}_{\mu\nu}^\dagger = \frac{1}{2} \langle \phi_\mu | e^{i\Lambda_{\mu\nu}} [\vec{\sigma} \cdot (\hat{\vec{p}} + \frac{1}{c}\hat{\vec{\mathcal{A}}}_\nu)] \ [\vec{\sigma} \cdot (\hat{\vec{p}} + \frac{1}{c}\hat{\vec{\mathcal{A}}}_\nu)] | \phi_\nu \rangle \tag{17}
$$

$$
\boldsymbol{\Pi}_{\mu\nu} = \frac{1}{2} \langle \phi_\mu | e^{i\Lambda_{\mu\nu}} [\vec{\sigma} \cdot (\hat{\vec{p}} + \frac{1}{c}\hat{\vec{\mathcal{A}}}_\nu)] \ [\vec{\sigma} \cdot (\hat{\vec{p}} + \frac{1}{c}\hat{\vec{\mathcal{A}}}_\nu)] | \phi_\nu \rangle \tag{18}
$$

$$
\boldsymbol{W}_{\mu\nu} = \langle \phi_\mu | e^{i\Lambda_{\mu\nu}} [\vec{\sigma} \cdot (\hat{\vec{p}} + \frac{1}{c}\hat{\vec{\mathcal{A}}}_\nu)] \hat{V} [\vec{\sigma} \cdot (\hat{\vec{p}} + \frac{1}{c}\hat{\vec{\mathcal{A}}}_\nu)] | \phi_\nu \rangle \tag{19}
$$

$$
\boldsymbol{T}_{\mu\nu} = \frac{1}{2} \langle \phi_\mu | e^{i\Lambda_{\mu\nu}} [\vec{\sigma} \cdot (\hat{\vec{p}} + \frac{1}{c}\hat{\vec{\mathcal{A}}}_\nu)] \ [\vec{\sigma} \cdot (\hat{\vec{p}} + \frac{1}{c}\hat{\vec{\mathcal{A}}}_\nu)] | \phi_\nu \rangle \tag{20}
$$

Here, the generalized momentum matrix $\boldsymbol{\Pi}$ and the small-small block of the metric $\boldsymbol{T}$ are identical due to the magnetically balanced basis set expansion. In a restricted kinetic balanced basis,[78] these matrices differ as $\boldsymbol{T}$ becomes independent of the vector potential. Note that the structure of these matrices is similar to those of NMR shielding constants.[66–68,70]

The four-component Dirac Hamiltonian can be reduced to a two-component form with a unitary transformation as suggested by Foldy and Wouthuysen[111]

$$
\mathbb{U}^\dagger \mathbb{D} \mathbb{U} = \begin{pmatrix} \boldsymbol{h}^+ & \mathbf{0}_2 \\ \mathbf{0}_2 & \boldsymbol{h}^- \end{pmatrix} \quad \text{with} \quad \mathbb{U}^\dagger \mathbb{U} = \mathbb{U}\mathbb{U}^\dagger = \mathbb{I}_4. \tag{21}
$$

Heully *et al.* later derived the explicit expression of the unitary matrix.[112] In X2C, this unitary transformation is carried out for the matrix representation of the Dirac Hamiltonian in one step. Therefore, the X2C Hamiltonian[32–38] in the presence of an external magnetic

8

field is then given by

$$h^+ = R^\dagger L R \tag{22}$$

with the matrix representation of the normalized elimination of the small component (NESC) operator[113–116]

$$L = V + X^\dagger \Pi + \Pi^\dagger X + X^\dagger \left(\frac{1}{4c^2} W - T \right) X \tag{23}$$

Note that all one-electron integrals explicitly depend on the external magnetic field due to the use of GIAOs. Moreover, Π, T, and W include a dependence on the magnetic field due to the restricted magnetic balance condition. The generalized momentum matrix Π is the only matrix, where the dependence also arises due to the generalized momentum operator $\hat{\vec{\pi}}$ and its vector potential $\hat{\vec{\mathcal{A}}}$. In X2C, the decoupling matrix X is computed based on a diagonalization of the Dirac matrix $\mathbb{D}$. The decoupling matrix reads

$$X = C_+^S (C_+^L)^{-1} \tag{24}$$

Additionally, the relativistic metric $\mathbb{M}$ needs to be transformed to the non-relativistic metric S. This introduces the renormalization matrix R, which allows one to integrate the resulting X2C Hamiltonian into the existing non-relativistic 1c or 2c infrastructure. The renormalization matrix is calculated as[37]

$$R = S^{-1/2} \left(S^{-1/2} \tilde{S} S^{-1/2} \right)^{-1/2} S^{1/2} \tag{25}$$

$$\tilde{S} = S + \frac{1}{2c^2} X^\dagger T X \tag{26}$$

using the metric of the large component $\tilde{S}$, for which the relation

$$C_{L+}^\dagger \, \tilde{S} \, C_{L+} = I \tag{27}$$

holds. This one-electron Hamiltonian is then commonly combined with the non-relativistic

two-electron interaction. Herein, we account for the missing two-electron picture-change correction with the modified screened nuclear spin–orbit (mSNSO) ansatz,[57,61,117,118] as this significantly improves the results for EPR parameters.[73,77]

2.4 Gauge-Invariant Formalism for EPR g-Tensors

The energy derivatives are now formed in the same manner as done in non-relativistic quantum chemistry. Thus, no derivatives of the density matrix are required.[119,120] Carrying out the energy derivative for the g-tensor in Eq. 2 consqeuently leads to working equations similar to two-component geometry gradients[57,58,121]

$$\frac{\mathrm{d}E}{\mathrm{d}B_u} = \mathrm{tr}\left[\boldsymbol{P}\left(\vec{J}_v\right)\boldsymbol{h}_u^B\right] + \frac{1}{2}\,\mathrm{tr}\left[\boldsymbol{G}\left(\vec{J}_v\right)\boldsymbol{\Gamma}_u^B\left(\vec{J}_v\right)\right] + E_{\mathrm{XC},u}^B\left(\vec{J}_v\right) - \mathrm{tr}\left[\boldsymbol{Z}\left(\vec{J}_v\right)\,\boldsymbol{S}_u^B\right] \quad (28)$$

Here, $\boldsymbol{P}$ and $\boldsymbol{G}$ are the one and two-electron density matrix, while $\boldsymbol{Z}$ is the energy-weighted density matrix.[119,120] $\boldsymbol{h}$ and $\boldsymbol{\Gamma}$ are the one-electron Hamiltonian and the two-electron integrals, respectively. E_{XC} is the exchange-correlation energy in density functional theory (DFT). The one-electron density matrix $\boldsymbol{P}$ reads

$$\boldsymbol{P} = \begin{pmatrix} \mathbf{P}^{\alpha\alpha} & \mathbf{P}^{\alpha\beta} \\ \mathbf{P}^{\beta\alpha} & \mathbf{P}^{\beta\beta} \end{pmatrix} \quad (29)$$

with the one-component matrices

$$\mathrm{Re}(P_{\mu\nu}^{\sigma_1\sigma_2}) = \sum_i n_i\left[\mathrm{Re}(c_{\mu i}^{\sigma_1})\,\mathrm{Re}(c_{\nu i}^{\sigma_2}) + \mathrm{Im}(c_{\mu i}^{\sigma_1})\,\mathrm{Im}(c_{\nu i}^{\sigma_2})\right] \quad (30)$$

$$\mathrm{Im}(P_{\mu\nu}^{\sigma_1\sigma_2}) = \sum_i n_i\left[-\,\mathrm{Re}(c_{\mu i}^{\sigma_1})\,\mathrm{Im}(c_{\nu i}^{\sigma_2}) + \mathrm{Im}(c_{\mu i}^{\sigma_1})\,\mathrm{Re}(c_{\nu i}^{\sigma_2})\right] \quad (31)$$

n_i is the occupation number of the corresponding two-component spinor and the superscript σ denotes the Kramers index ($\sigma = \alpha, \beta$). $c_{\mu i}$ are the spinor coefficients from a self-consistent field (SCF) procedure. The two-electron density matrix is formed similarly.[121] Note that

these matrices are constructed from the spinors with $\vec{J}$ aligned along the v axis. As $\boldsymbol{S}_u^B$ is an antisymmetric and purely imaginary matrix, which is diagonal in the (2×2) superspace, we only need the respective $\alpha\alpha$ and $\beta\beta$ blocks of the energy-weighted density matrix, given by the spinor coefficients and energies, according to

$$\mathrm{Im}\left[\mathbf{Z}_{\mu\nu}^{\sigma\sigma}\right] = \sum_i n_i \left[-\mathrm{Re}(c_{\mu i}^\sigma)\epsilon_i \mathrm{Im}(c_{\nu i}^\sigma) + \mathrm{Im}(c_{\mu i}^\sigma)\epsilon_i \mathrm{Re}(c_{\nu i}^\sigma) \right] \tag{32}$$

n_i is the occupation number. Therefore, the last term in Eq. 28 is simplified to

$$\mathrm{tr}\left(\boldsymbol{Z}\boldsymbol{S}_u^B\right) = -\mathrm{tr}\left(\mathrm{i}\left\{\mathrm{Im}\left[\mathbf{Z}^{\alpha\alpha}\right] + \mathrm{Im}\left[\mathbf{Z}^{\beta\beta}\right]\right\}\mathbf{S}_u^B\right) \tag{33}$$

Note that the imaginary part of the energy-weighted density matrix is not needed for relativistic geometry gradients. However, it also arises for geometry gradients in finite magnetic fields.[122] An important point is that all terms in Eq. 28 except for the one with $\boldsymbol{h}_u^B$ arise solely due to the basis set expansion with GIAOs. Note that the computation of the two-electron integral derivatives is described in Refs. 123–125 and their generalization to a two-component framework is carried out as described in, e.g., Refs. 121 and 126. Further note that the derivatives of the two-electron integrals in Eq. 28 are known from the right-hand side of the coupled-perturbed Hartree–Fock (CPHF) or Kohn–Sham (CPKS) equations for two-component NMR shielding tensors.[68,88,90,91,127] The crucial part for a relativistic treatment is the derivative of the one-electron Hamiltonian, which is also very similar to the perturbed density contribution or paramagnetic contribution to the NMR shielding tensor.[66–68,70,128]

Generally, the X2C Hamiltonian derivatives are given by

$$\boldsymbol{h}_u^{+,B} = \boldsymbol{R}_u^{\dagger,B}\boldsymbol{L}\boldsymbol{R} + \boldsymbol{R}^\dagger\boldsymbol{L}_u^B\boldsymbol{R} + \boldsymbol{R}^\dagger\boldsymbol{L}\boldsymbol{R}_u^B \tag{34}$$

where the derivative of the NESC matrix reads

$$
\begin{aligned}
\boldsymbol{L}_u^B = \quad & \boldsymbol{V}_u^B + \boldsymbol{\Pi}_u^{\dagger,B}\boldsymbol{X} + \boldsymbol{\Pi}^\dagger\boldsymbol{X}_u^B + \boldsymbol{X}_u^{\dagger,B}\boldsymbol{\Pi} + \boldsymbol{X}^\dagger\boldsymbol{\Pi}_u^B \\
& + \boldsymbol{X}_u^{\dagger,B}\left(\frac{1}{4c^2}\boldsymbol{W} - \boldsymbol{T}\right)\boldsymbol{X} + \boldsymbol{X}^\dagger\left(\frac{1}{4c^2}\boldsymbol{W}_u^B - \boldsymbol{T}_u^B\right)\boldsymbol{X} + \boldsymbol{X}^\dagger\left(\frac{1}{4c^2}\boldsymbol{W} - \boldsymbol{T}\right)\boldsymbol{X}_u^B
\end{aligned}
\tag{35}
$$

Thus, the one-electron integral derivatives of all matrices involved in the NESC matrix are needed. Additionally, the derivative of the overlap matrix is required for $\boldsymbol{R}_u^B$ (*vide infra*) The derivatives of the potential and the overlap are

$$
\left(\frac{\partial\mathbf{V}_{\mu\nu}}{B_u}\right)_0 = \frac{\mathrm{i}}{2c}\langle\lambda_\mu|(\vec{R}_{\mu\nu}\times\hat{\vec{r}})_u\,\hat{V}|\lambda_\nu\rangle
\tag{36}
$$

$$
\left(\frac{\partial\mathbf{S}_{\mu\nu}}{B_u}\right)_0 = \frac{\mathrm{i}}{2c}\langle\lambda_\mu|(\vec{R}_{\mu\nu}\times\hat{\vec{r}})_u|\lambda_\nu\rangle
\tag{37}
$$

These derivatives are purely imaginary and antisymmetric. Moreover, they are identical to the one-component non-relativistic integral derivatives. The other derivatives are not block-diagonal in the 2c space and read[66–68,70]

$$
\left(\frac{\partial\boldsymbol{T}_{\mu\nu}}{\partial B_u}\right)_0 = \frac{\mathrm{i}}{4c}\sigma_0\langle\lambda_\mu|(\vec{R}_{\mu\nu}\times\hat{\vec{r}})_u\,\hat{\vec{p}}\,^2|\lambda_\nu\rangle + \frac{1}{2c}\sigma_0\langle\lambda_\mu|(\hat{\vec{r}}_\nu\times\hat{\vec{p}})_u|\lambda_\nu\rangle + \frac{1}{2c}\sigma_u\langle\lambda_\mu|\lambda_\nu\rangle \tag{38}
$$

$$
\left(\frac{\partial\boldsymbol{\Pi}_{\mu\nu}^\dagger}{\partial B_u}\right)_0 = \frac{\mathrm{i}}{4c}\sigma_0\langle\lambda_\mu|(\vec{R}_{\mu\nu}\times\hat{\vec{r}})_u\,\hat{\vec{p}}\,^2|\lambda_\nu\rangle + \frac{1}{2c}\sigma_0\langle\lambda_\mu|(\hat{\vec{r}}_\nu\times\hat{\vec{p}})_u|\lambda_\nu\rangle + \frac{1}{2c}\sigma_u\langle\lambda_\mu|\lambda_\nu\rangle \tag{39}
$$

$$
\begin{aligned}
\left(\frac{\partial\boldsymbol{W}_{\mu\nu}}{\partial B_u}\right)_0 = \quad & \frac{\mathrm{i}}{2c}\sigma_0\langle\lambda_\mu|(\vec{R}_{\mu\nu}\times\hat{\vec{r}})_u\,\hat{\vec{p}}\cdot\hat{V}\hat{\vec{p}}|\lambda_\nu\rangle + \frac{1}{2c}\sigma_0\langle\lambda_\mu|(\hat{\vec{r}}_\nu\times\hat{\vec{p}})_u\,\hat{V} + \hat{V}\,(\hat{\vec{r}}_\nu\times\hat{\vec{p}})_u|\lambda_\nu\rangle \\
& + \frac{1}{2c}\langle\lambda_\mu|(\vec{R}_{\mu\nu}\times\hat{\vec{r}})_u\,\mathrm{i}\vec{\sigma}\cdot\left(\hat{\vec{p}}\times\hat{V}\hat{\vec{p}}\right)|\lambda_\nu\rangle + \frac{1}{c}\sigma_u\langle\lambda_\mu|\hat{V}|\lambda_\nu\rangle \\
& + \langle\lambda_\mu|\frac{\mathrm{i}}{2c}\sigma_u\left(\hat{\vec{p}}\,\hat{V}\right)\cdot\hat{\vec{r}}_\nu - \frac{\mathrm{i}}{2c}\left(\hat{\vec{p}}\,\hat{V}\right)_u\left(\vec{\sigma}\cdot\hat{\vec{r}}_\nu\right)|\lambda_\nu\rangle
\end{aligned}
\tag{40}
$$

The expressions for the derivatives of $\boldsymbol{T}$ and $\boldsymbol{\Pi}$ are obtained by making use of the commutator for $\hat{\vec{r}}$ and $\hat{\vec{p}}$. Note that the first-order Dirac matrix is still Hermitian. The spin-free part of all matrices is antisymmetric and purely imaginary. The spin-dependent contributions of the relativistically modified potential $\boldsymbol{W}$ and its derivatives are rescaled in the (modified)

screened nuclear spin-orbit approach (SNSO, mSNSO).[57,61,117,118] Note that we apply the SNSO and mSNSO to the integrals directly.[129]

The derivatives of the decoupling matrix $\boldsymbol{X}_u^B$ are obtained using one-electron response theory as reviewed in the appendix of Ref. 70. We refer to this reference for a detailed derivation and overview of related approaches. The working equations are

$$\boldsymbol{X}_u^B = \left(\boldsymbol{C}_-^S - \boldsymbol{X}\boldsymbol{C}_-^L\right) \ \left(\boldsymbol{U}_u^B\right)_{-+} \ \boldsymbol{C}_+^{L,\dagger} \ \tilde{\boldsymbol{S}} \tag{41}$$

with the orbital rotation matrix

$$(\boldsymbol{U}_{u,-+}^B)_{kl} = \frac{(\tilde{\boldsymbol{D}}_{u,-+}^B)_{kl} - (\tilde{\boldsymbol{M}}_{u,-+}^B)_{kl} \ (\boldsymbol{E}_{++})_{ll}}{(\boldsymbol{E}_{++})_{ll} - (\boldsymbol{E}_{--})_{kk}} \tag{42}$$

The derivatives of the Dirac matrix and the metric of Eq. 14 are transformed to the basis of the unperturbed solutions according to

$$\begin{aligned}
\tilde{\boldsymbol{D}}_{u,-+}^B &= \ \ \boldsymbol{C}_-^{L,\dagger}\boldsymbol{V}_u^B\boldsymbol{C}_+^L + \boldsymbol{C}_-^{L,\dagger}\boldsymbol{\Pi}_u^{\dagger,B}\boldsymbol{C}_+^S + \boldsymbol{C}_-^{S,\dagger}\boldsymbol{\Pi}_u^B\boldsymbol{C}_+^L \\
&\quad + \frac{1}{4c^2}\boldsymbol{C}_-^{S,\dagger}\boldsymbol{W}_u^B\boldsymbol{C}_+^S - \boldsymbol{C}_-^{S,\dagger}\boldsymbol{T}_u^B\boldsymbol{C}_+^S \tag{43} \\
\tilde{\boldsymbol{M}}_{u,-+}^B &= \ \boldsymbol{C}_-^{L,\dagger}\boldsymbol{S}_u^B\boldsymbol{C}_+^L + \frac{1}{2c^2}\boldsymbol{C}_-^{S,\dagger}\boldsymbol{T}_u^B\boldsymbol{C}_+^S \tag{44}
\end{aligned}$$

The derivatives of the renormalization matrix are calculated by solving the Sylvester matrix equation

$$\boldsymbol{R}\boldsymbol{R}_u^B + \boldsymbol{R}_u^B\boldsymbol{R} = \tilde{\boldsymbol{S}}^{-1}\left(\mathrm{S}_u^B - \tilde{\boldsymbol{S}}_u^B\boldsymbol{R}\boldsymbol{R}\right) \tag{45}$$

using a generalized eigenvalue decomposition method.[56] The derivative of $\tilde{\boldsymbol{S}}$ is given by

$$\tilde{\boldsymbol{S}}_u^B = \boldsymbol{S}_u^B + \frac{1}{2c^2}\boldsymbol{X}_u^{\dagger,B}\boldsymbol{T}\boldsymbol{X} + \frac{1}{2c^2}\boldsymbol{X}^\dagger\boldsymbol{T}_u^B\boldsymbol{X} + \frac{1}{2c^2}\boldsymbol{X}^\dagger\boldsymbol{T}\boldsymbol{X}_u^B \tag{46}$$

These Sylvester matrix equations are obtained by differentiating the quadratic expression

for the renormalization matrix[116]

$$RR = \tilde{S}^{-1}S \tag{47}$$

with respect to the magnetic field. The simplification of this formalism with a common gauge origin and the RKB condition is discussed in the appendix A. There, we also outline how our EPR implementation can be used for paramagnetic NMR (pNMR) shielding tensors.

2.5 Local Approximation to the X2C Hamiltonian

All X2C steps are carried out in the uncontracted or primitive basis set. Thus, the $\mathcal{O}(N^3)$ scaling of the diagonalization may limit the applicability of X2C for very large molecular systems.[101] Here, N denotes the number of basis functions. Therefore, local approximations are commonly introduced.[100] Herein, we chose the diagonal local approximation to the unitary decoupling transformation.[99] In DLU, the unitary decoupling transformation matrix $\mathbb{U}$ is approximated as a direct sum of atomic contributions according to[58]

$$U^{\mathrm{LL}} \;=\; \bigoplus_A U_{AA}^{\mathrm{LL}} = \bigoplus_A R_{AA} \tag{48}$$

$$U^{\mathrm{SL}} \;=\; \bigoplus_A U_{AA}^{\mathrm{SL}} = \bigoplus_A X_{AA} R_{AA} \tag{49}$$

Note that the (relativistically modified) potential still includes the sum over all nuclei. We denote an atomic diagonal block AA and a general block AB, where the atomic blocks are formed according to the atom centers of the basis functions of the respective matrix elements. Therefore, the Hamiltonian is simplified to

$$
\begin{aligned}
h_{AB}^+ =\;\; & R_{AA}^\dagger \left(V_{AB} + \Pi_{AB}^\dagger X_{BB} + X_{AA}^\dagger \Pi_{AB} \right) R_{BB} \\
& + R_{AA}^\dagger \left(X_{AA}^\dagger \left[\frac{1}{4c^2} W_{AB} - T_{AB} \right] X_{BB} \right) R_{BB}
\end{aligned} \tag{50}
$$

Analytical derivatives are formed with the product rule. Thus, only the atomic diagonal block of X and R as well as their derivatives are required. However, both the atomic

14

diagonal and atomic off-diagonal blocks of the integral derivatives are needed according to

$$
\begin{aligned}
\boldsymbol{h}_{AB}^{+,B} = \ & \boldsymbol{R}_{AA,u}^{\dagger,B} \boldsymbol{L}_{AB} \boldsymbol{R}_{BB}^{\dagger} + \boldsymbol{R}_{AA}^{\dagger} \boldsymbol{L}_{AB} \boldsymbol{R}_{BB,u}^{B} \\
& + \boldsymbol{R}_{AA}^{\dagger} \left(\boldsymbol{V}_{AB,u}^{B} + \boldsymbol{\Pi}_{AB,u}^{\dagger,B} \boldsymbol{X}_{BB} + \boldsymbol{X}_{AA}^{\dagger} \boldsymbol{\Pi}_{AB,u}^{B} \right) \boldsymbol{R}_{BB} \\
& + \boldsymbol{R}_{AA}^{\dagger} \left(\boldsymbol{\Pi}_{AB}^{\dagger} \boldsymbol{X}_{BB,u}^{B} + \boldsymbol{X}_{AA,u}^{\dagger,B} \boldsymbol{\Pi}_{AB} \right) \boldsymbol{R}_{BB} \\
& + \boldsymbol{R}_{AA}^{\dagger} \left(\boldsymbol{X}_{AA,u}^{\dagger,B} \left[\frac{1}{4c^2} \boldsymbol{W}_{AB} - \boldsymbol{T}_{AB} \right] \boldsymbol{X}_{BB} \right) \boldsymbol{R}_{BB} \\
& + \boldsymbol{R}_{AA}^{\dagger} \left(\boldsymbol{X}_{AA}^{\dagger} \left[\frac{1}{4c^2} \boldsymbol{W}_{AB} - \boldsymbol{T}_{AB} \right] \boldsymbol{X}_{BB,u}^{B} \right) \boldsymbol{R}_{BB} \\
& + \boldsymbol{R}_{AA}^{\dagger} \left(\boldsymbol{X}_{AA}^{\dagger} \left[\frac{1}{4c^2} \boldsymbol{W}_{AB,u}^{B} - \boldsymbol{T}_{AB,u}^{B} \right] \boldsymbol{X}_{BB} \right) \boldsymbol{R}_{BB}
\end{aligned}
\tag{51}
$$

3   Implementation

The calculation of EPR g-tensors with a common gauge origin is implemented into the ridft module[58,101,121,126,130–132] of TURBOMOLE.[48,133–135] Here, the g-tensor is evaluated after the SCF iterations. The gauge-invariant ansatz employing GIAOs is implemented into the mp-shift module.[124,125,136–138] The spin-independent integral derivatives using GIAOs are taken from Ref. 70. All new integrals are implemented using a combination of Gauss–Hermite and Gauss–Rys integration[139–142] as done previously for other magnetic[71,73,74] and electric properties.[143] The finite nucleus model is available throughout using the finite nucleus exponents of Ref. 144. The (modified) screened-nuclear spin–orbit (SNSO, mSNSO) approximation is available for the spin-dependent integral (derivatives) of the relativistically modified potential $\boldsymbol{W}$.[57,61,117,118] The response and Sylvester matrix equations are solved by a generalization of the existing one-component routines[70] as done previously for the HFC constant[73] and NMR coupling constants.[71] As our previous works, the implementation is fully integral direct. We use $c = 137.0359990840$ a.u.[145] for the speed of light in atomic units. Additional contributions from point charges or the conductor-like screening model[146,147] (COSMO) arise due to the use of GIAOs and are treated without relativistic picture-change correction. Thus, we use the available non-relativistic implementation[125] for these terms.

The ridft module supports the (multipole-accelerated) resolution of the identity approximation (MARI-J, RI-J, and RI-K) throughout.[126,148] Additionally, the seminumerical exchange approximation is available.[130,131] The mpshift module only supports MARI-J and RI-J for integral derivatives.[125] Note that these do not require changes for a two-component ansatz as the Coulomb term depends on the total density.[126] The analytical exchange integral derivatives with respect to the magnetic fields[124] are extended to a two-component framework as done previously for energies[126] and energy gradients.[121] Therefore, the integral routines are able to process the eight density matrices. For the contraction with the density matrix, we construct the symmetric and antisymmetric linear combinations.[121]

Density functional approximations are available up to the fourth rung of Jacob's ladder.[149–151] The kinetic energy density τ is generalized using the external magnetic field as suggested by Maximoff and Scuseria.[152] Interfaces to Libxc[153–155] and XCFun[156] are provided. For this work, the existing one-component implementations[125,136,157] are extended like done previously for the SCF energy.[126] Thus, the non-collinear exchange-correlation energy depends on the total density matrix $\mathbf{M}_0$ and the three spin vector density matrices $\mathbf{M}_i(i = x, y, z)$. These are defined as[108,158]

$$\mathbf{M}_0 = \mathrm{Re}(\mathbf{P}^{\alpha\alpha}) + \mathrm{Re}(\mathbf{P}^{\beta\beta}) \tag{52}$$

$$\mathbf{M}_x = \mathrm{Re}(\mathbf{P}^{\alpha\beta}) + \mathrm{Re}(\mathbf{P}^{\beta\alpha}) \tag{53}$$

$$\mathbf{M}_y = \mathrm{Im}(\mathbf{P}^{\alpha\beta}) - \mathrm{Im}(\mathbf{P}^{\beta\alpha}) \tag{54}$$

$$\mathbf{M}_z = \mathrm{Re}(\mathbf{P}^{\alpha\alpha}) - \mathrm{Re}(\mathbf{P}^{\beta\beta}) \tag{55}$$

The XC potential follows as

$$\boldsymbol{V}_{\mathrm{XC}}[M_0(\vec{r}), M_i(\vec{r})] = \frac{\delta E_{\mathrm{XC}}[M_0(\vec{r}), \rho_i(\vec{r})]}{\delta M_0(\vec{r})} + \vec{\sigma}_i \frac{\delta E_{\mathrm{XC}}[M_0(\vec{r}), M_i(\vec{r})]}{\delta M_i(\vec{r})} \tag{56}$$

and the existing one-component implementation[125,136,157] can be extended straightforwardly

based on the existing energy routines.[126]

All algebraic operations, transformations, and integral evaluations are parallelized using the OpenMP scheme[159,160] and we use the Intel® Math Kernel Library (Intel MKL) throughout this work. Preparation and post-processing scripts are available based on our previous endeavors for the hyperfine coupling matrix.[73] Three independent calculations based on converged unrestricted Kohn–Sham (UKS) or Hartree–Fock (UHF) orbitals are needed to obtain the complete EPR g-matrix. This matrix is then transformed into its principal axis system, where the g-matrix is diagonal, either through constructing the rank-2 tensor $\left(\boldsymbol{gg}^{\mathrm{T}} \right)$ and subsequently diagonalizing, or by diagonalization of the symmetric part, which is given by $1/2 \left(\boldsymbol{g} + \boldsymbol{g}^{\mathrm{T}} \right)$. We implemented both ansätze using Python scripts.

4   Computational Details

To begin, we compare our newly developed X2C implementation to established two-component DKH and ZORA approaches. A small set of 11 molecules, i.e. RhC, PdH, ZnH, CdH, HgH, ZnF, CdF, HgF, ZnAg, CdAg, and HgAg, is selected. This set was previously studied with DKH and a common gauge origin in Ref. 27 as well as with ZORA and GIAOs in Ref. 161. For consistency, we use the bond lengths collected in the latter reference. Both the DKH and ZORA calculations are performed with tailored basis sets and the BP86 functional.[162,163] Note that the ZORA study is carried out with Slater-type orbitals. Consequently, we also apply basis sets optimized for X2C—namely the x2c-QZVPall-2c basis set[164] herein. Additionally, we employ the uncontracted Dyall-VTZ basis set for Rh, Pd, Ag, Cd, and Hg,[165–168] while the decontracted pcS-2 basis is used for H and F.[169] For Zn, the decontracted pcSseg-2 bases[170] are chosen. Results with this basis set combination are listed in the Supporting Information. Additionally, results with the PBE0[171,172] and ωB97X-D[173] functionals as well as results with the RKB and RMB condition using a common gauge origin are provided in the Supporting Information. The impact of the structure on the g-tensor is also studied in

the Supporting Information. Tight SCF thresholds of $10^{-8}\,E_h$ and fine grids[174–176] (grid 4a) are applied. The shift of the principal components of the g-tensor is given relative to the free electron in parts per thousand (ppt), $\Delta g = (g - g_e) \cdot 1000$.

Furthermore, we perform benchmark calculations to assess the three parameters of a quantum chemical DFT calculation of the g-tensor—namely the Hamiltonian, the basis set, and the density functional approximation (DFA). This complements our previous work on the HFC constant.[73] First, we consider the 17 transition-metal complexes of Ref. 29, namely $[MoNCl_4]^{2-}$, $[MoOF_4]^-$, $[MoOCl_4]^-$, $[MoOF_5]^{2-}$, $[MoOBr_5]^{2-}$, $[WOCl_4]^-$, $[WOF_5]^{2-}$, $[WOBr_5]^{2-}$, $[TcNF_4]^-$, $[TcNCl_4]^-$, $[TcNBr_4]^-$, $[ReNF_4]^-$, $[ReNCl_4]^-$, $[ReNBr_4]^-$, $[ReOBr_4]$, $[ReOF_5]^-$, and $[OsOF_5]$, and compare our X2C and DLU-X2C results to available 4c reference data. In line with that reference, we use the RKB condition for the basis set expansion and a common gauge origin placed at the heavy atom center. Decontracted IGLO-III bases are employed for the light elements, namely N, F, and Cl,[177] while the Dyall-VTZ basis set is used for Br[165,168] and the Dyall-TZ bases for Mo, Tc, W, Re, and Os.[166–168] The PBE0[171,172] functional is chosen with very large grids (grid 5a).[174–176] Furthermore, the mSNSO approximation is applied and an SCF convergence threshold of $10^{-9}\,E_h$ is selected. Results without the mSNSO approximation are presented in the Supporting Information. There, we also discuss the impact of diffuse basis functions using the Sapporo-DKH3-QZP-2012-diffuse bases.[178,179] All two-component calculations are performed with converged UKS orbitals. In this work, "PCC" indicates that the derivatives of the decoupling and the renormalization matrices are neglected. Thus, the computational algorithm becomes similar to ordinary picture-change corrections of expectation values.[143] Like Ref. 29, we use the shift Δg in ppt relative to the g-factor of the free electron. The impact of the balance condition and the gauge-invariant formalism is assessed for the same set of molecules using the described computational settings.

Second, the importance of the basis set is studied. To do so, the basis sets in Tab. 1 are considered. The x2c-SVPall-2c-s and x2c-TZVPall-2c-s bases are obtained by combining

18

the extensions for NMR shieldings of Ref. 176 with the 2c extensions of Ref. 132. Note that the comparably flat p and d functions of the NMR extensions were removed to avoid linear dependencies, as these functions were optimized to serve as a minimal version of the 2c extensions.[176] For convenience, the basis sets are given as part of the Supporting Information. We measure the errors with respect to the large even-tempered basis set of Ref. 164. Note that $[TcNCl_4]^-$ (4 ppt) and $[WOF_5]^{2-}$ are excluded form the statistical evaluation. Only the DLU-X2C Hamiltonian using the RMB-GIAO approach is discussed in the main text and we refer to the Supporting Information for the results with the CGO ansatz.

Table 1: Considered basis sets and basis set combinations for the light (N, O, F, Cl) and heavy elements (Br, Mo, Tc, W, Re, Os). The suffix "-unc" denotes that the bases are used in the decontracted form. NBF is the total number of spherical AO basis functions. The even-tempered reference basis set[176] uses 26085 basis functions for the molecular test set (average: 1534). "Avg." denotes the average number of basis functions for a molecule.

Basis Set	Light Elements	Ref.	Heavy Elements	Ref.	NBF	Avg.
1	IGLO-II-unc	177	Dyall-VDZ-unc	165–168	6421	378
2	IGLO-III-unc	177	Dyall-VTZ-unc	165–168	9176	540
3	pcS-1-unc	169	Dyall-VDZ-unc	165–168	6742	397
4	pcS-2-unc	169	Dyall-VTZ-unc	165–168	10140	596
5	pcS-3-unc	169	Dyall-VQZ-unc	165–168	15217	895
6	cc-pVDZ-unc	180,181	Dyall-VDZ-unc	165–168	6440	379
7	cc-pVTZ-unc	180,181	Dyall-VTZ-unc	165–168	9425	554
8	cc-pVQZ-unc	180,181	Dyall-VQZ-unc	165–168	11634	684
9	Sapporo-DZP-2012	178	Sapporo-DKH3-DZP-2012	178,179	3369	198
10	Sapporo-TZP-2012	178	Sapporo-DKH3-TZP-2012	178,179	6213	367
11	Sapporo-QZP-2012	178	Sapporo-DKH3-QZP-2012	178,179	9804	577
12	Jorge-DZP-DKH	182	Jorge-DZP-DKH	182–184	3085	181
13	Jorge-TZP-DKH	182	Jorge-TZP-DKH	182–184	5038	296
14	x2c-SVPall-2c	132	x2c-SVPall-2c	132	3315	195
15	x2c-TZVPall-2c	132	x2c-TZVPall-2c	132	5095	300
16	x2c-QZVPall-2c	164	x2c-QZVPall-2c	164	8799	518
17	x2c-SVPall-2c-s	132,176	x2c-SVPall-2c-s	132,176	3671	216
18	x2c-TZVPall-2c-s	132,176	x2c-TZVPall-2c-s	132,176	5427	319
16	x2c-QZVPall-2c-s	164	x2c-QZVPall-2c-s	164	8946	526
20	x2c-SVPall-2c-unc	132	x2c-SVPall-2c-unc	132	7614	448
21	x2c-TZVPall-2c-unc	132	x2c-TZVPall-2c-unc	132	9104	536
22	x2c-QZVPall-2c-unc	164	x2c-QZVPall-2c-unc	164	14366	845
23	ANO-R-unc	185	ANO-R-unc	185	15764	927
24	ANO-RCC-unc	186	ANO-RCC-unc	186,187	15757	927

Third, we study common density functional approximations. As representatives for pure functionals, we choose S-VWN,[188–190] KT3,[191] BP86,[162,163] PBE,[171] TPSS,[192] revTPSS,[193,194] and r^{2}SCAN.[195,196] BH&HLYP,[163,197,198] B3LYP,[197,199] PBE0,[171,172] a modified version of PBE0 including 40% of Hartree–Fock (HF) exchange (PBE0-40HF),[29,171,172] B97,[200] B97-2,[201] TPSSh,[202] revTPSSh,[193,194] and TPSS0 [202,203] are selected to cover frequently used global hybrid functionals. For common range-separated hybrids, we employ the CAM-B3LYP,[204] CAM-QPT-00,[205] CAM-QTP-02,[206] HSE06,[207–209] LC-ωPBE,[210] and ωB97X-D [173] functionals. Libxc [153–155] is used for the range-separated hybrid functionals, KT3, revTPSS(h), TPSS0, r^{2}SCAN, and B97 throughout this work. We use XCFun [156] for PBE0-40HF. Additionally, Hartree–Fock calculations are performed. COSMO is employed with the default parameters to compensate the negative charge [146,147] and the x2c-QZVPall-2c basis set is chosen for consistency with our previous studies on the HFC constant.[73] Note that COSMO introduces additional integral derivatives due to the GIAOs. Errors are measured with respect to the experimental findings [211–222] collected in Ref. 29.

Fourth, we apply the mSNSO-DLU-X2C Hamiltonian and the three ansätze to the larger complex [Pt(C$_6$Cl$_5$)$_4$]$^-$. We chose the position of Pt as the common gauge origin for the RKB-CGO and RMB-CGO approaches. The structure is taken from Ref. 29 and we employ COSMO with the default parameters.[146,147,223] BH&HLYP,[163,197,198] B3LYP,[197,199] PBE0,[171,172] PBE0-40HF,[29,171,172] TPSSh,[202] TPSS0,[202,203] CAM-B3LYP,[204] CAM-QPT-00,[205] CAM-QTP-02,[206] HSE06,[207–209] LC-ωPBE,[210] and ωB97X-D [173] are considered. Fine grids (grid 4a) are used for the numerical integration of the XC parts.[174–176] The uncontracted Dyall-VTZ basis [224] is combined with the decontracted pcS-2 basis.[169] We use the universal (uncontracted) x2c-type fitting bases [132,164] for the RI-J approximation in the 2c calculations.[126] Furthermore, the x2c-QZVPall-2c basis [164] is applied together with the tailored auxiliary basis.[132,164] An SCF threshold of 10^{-8} E$_h$ is selected. In total, the number of basis functions in the spherical atomic orbital representation amounts to 3360 (Dyall-VTZ-unc/pcS-2-unc) and 3003 (x2c-QZVPall-2c, 4720 primitive functions).

In Sec. 7, we study the three lanthanide molecules [La(OAr*)$_3$]$^-$, [Lu(NR$_2$)$_3$]$^-$, and [Lu(OAr*)$_3$]$^-$ (OAr* = 2,6-Ad$_2$-4-t-Bu-C$_6$H$_2$O, Ad = adamantyl, t-Bu= tert-butyl, R = SiMe$_3$ with Me = methyl) of Ref. 8 using the structures provided therein. The g-tensors are calculated with the x2c-SVPall-2c basis set for the light elements[132] and the x2c-TZVPPall-2c[132] or x2c-QZVPall-2c basis[164] for La and Lu. The mSNSO-DLU-X2C Hamiltonian is applied and we employ the TPSS,[192] r^{2}SCAN,[195,196] PBE0,[171,172] PBE0-40HF,[29,171,172] CAM-QTP-02,[206] HSE06,[207–209] and ωB97X-D[173] functionals with fine grids (grid 4a).[174–176] Here, we apply COSMO to treat the molecular environment in solution.[146,147] Thus, we use the respective parameters for tetrahydrofuran (THF), which are $\epsilon_r = 7.520$, a solvation radius of 1.30 Å, and a refractive index of 1.4050. The SCF procedure is considered converged with an energy threshold of 10^{-7} E$_h$ and criterion of 10^{-7} a.u. for the root mean square of the density matrix. The common gauge origin is placed at the La or Lu atom.

5   Comparison to other Two-Component Approaches for Diatomic Molecules

The Δg shifts of diatomic molecules at various two-component levels are shown in Tab. 2. Our gauge-invariant X2C framework is compared to the non-collinear DKH approach of Malkin et al.[27] and the ZORA Hamiltonian.[161] All 11 molecules feature a Kramers doublet ground state. Overall, the X2C and DKH Hamiltonian lead to qualitatively similar results. For HgH, the largest absolute deviations are observed with 14.6 ppt (Δg$_\perp$). The ZORA results show a larger deviation towards X2C or DKH. Here, the deviation amounts to more than 60 ppt for PdH. This behavior can be rationalized by the closer formal relationship of X2C and DKH as well as the use of Gaussian-type orbitals. Note that the ZORA implementation[23,161] utilizes Slater-type orbitals, and thus the basis sets cannot be compared directly. Moreover, both the X2C and DKH ansatz make use of three non-collinear calculations to assemble the complete g-tensor. Notably, this framework includes spin polarization. In contrast to DKH, magnetic

Table 2: Principal components of the Δg shift in ppt for a set of diatomic molecules compiled in Ref. 161. Our gauge-invariant mSNSO-X2C approach is compared to the DKH ansatz with a common gauge origin of Ref. 27 and the ZORA formalism using GIAOs of Ref. 161. These corresponding results are taken from these references. Note that all calculations use tailored basis sets for the respective Hamiltonian and the BP86 functional. X2C results with the uncontracted Dyall-VTZ/pcS-2 basis and more sophisticated functionals are given in the Supporting Information. $\parallel$ and $\perp$ refer to the components of the g-tensor parallel and perpendicular to the bond axis. Experimental (Expt.) results are taken from Ref. 226.

Molecule	X2C-GIAO		DKH-CGO		ZORA-GIAO		Expt.	
	$\Delta g_{\parallel}$	$\Delta g_{\perp}$	$\Delta g_{\parallel}$	$\Delta g_{\perp}$	$\Delta g_{\parallel}$	$\Delta g_{\perp}$	$\Delta g_{\parallel}$	$\Delta g_{\perp}$
RhC	−3.0	53.6	−0.6	56.9	−2.0	50.3	1.6	51.8
PdH	−22.6	230.2	−16.5	224.2	−27.7	294.8	−37.3	290.9
ZnH	−2.5	−23.6	−0.3	−19.1	−0.4	−24.9	−2.0	−17.1
CdH	−4.1	−62.1	−1.9	−59.8	−2.4	−71.7	−5.3	−49.9
HgH	−25.0	−221.9	−25.9	−236.5	−30.0	−251.8	−26.3	−174.3
ZnF	−2.3	−9.2	−0.3	−6.7	−0.3	−6.8	−0.3	−6.3
CdF	−2.7	−22.4	−0.8	−21.2	−0.9	−21.4	−1.3	−17.3
HgF	−13.3	−50.0	−11.6	−54.1	−14.0	−66.1	−9.3	−41.3
ZnAg	−2.2	−20.6	−0.2	−19.0	−0.3	−21.8	0.2	−11.8
CdAg	−3.1	−46.9	−1.1	−45.9	−1.3	−51.3	−0.9	−31.2
HgAg	−10.7	−131.8	−10.0	−140.9	−10.4	−143.8	−6.5	−88.7

properties can be formulated straightforwardly in X2C. For instance, a back transformation of the DKH wave function to the 4c picture is applied to (approximately) arrive at the DKH-transformed expression of the first-order Zeeman operator in Ref. 27. A detailed discussion of magnetic fields in DKH and the associated difficulties is provided in Ref. 225.

All calculations utilize the generalized gradient approximation (GGA) functional BP86 and therefore a comparison with the experimental findings reveals notable deviations for some molecules. For instance, all methods fail to predict the correct sign of the $\Delta g_{\parallel}$ shift for RhC. Also for PdH, HgH, and HgAg, the experimental results are not accurately reproduced. As shown by further studies in the Supporting Information, this can be reduced by choosing more sophisticated functionals such as PBE0 and ωB97X-D, while the uncontracted Dyall-VTZ/pcS-2 bases lead to very similar results. Further improvements are obtained when optimizing the structure at the same level of theory as for the calculation of the g-tensor.

Especially for PdH, this protocol results in a major improvement. The components of the g-tensor change to -33.2 ppt and 315.4 ppt, which is much closer to the experimental findings of -37.3 ppt and 290.9 ppt.

6 Assessment for Transition-Metal Complexes

In this section, we first assess the accuracy of the relativistic Hamiltonian in Sec. 6.1. Then, the importance of the basis set is discussed in Sec. 6.2. Lastly, various density functional approximations are considered in Sec. 6.3. We only discuss the RMB-GIAO approach for the basis set and the density functional approximation in the main text. We refer to the Supporting Information for the other approaches.

6.1 Comparison to Four-Component Data and Hamiltonian Studies

The X2C and DLU-X2C Hamiltonian are further assessed by comparison to the 4c Hamiltonian for the 17 transition-metal complexes in Tab. 3. First, the quasi-relativistic Hamiltonians accurately reproduce the 4c results. Even for the W, Re, and Os compounds, the deviation of the isotropic Δg shift towards the 4c results amounts to at most 4 ppt. For the Mo and Tc complexes, the deviation is below 2 ppt and often even below 1 ppt. Similar trends are observed for the three principal components. We discuss the impact of the mSNSO approach on the results in detail in the Supporting Information. Here, we just state that it results in a substantial improvement. Generally, the calculated g-tensors are in good agreement with the experimental findings for the Mo, W, and Os complexes. Here, the deviation amounts to at most 10 ppt for $[MoOF_4]^-$ and 15 ppt for both $[WOBr_5]^{2-}$ and $[OsOF_5]$. Given the absolute value of the isotropic Δg shift for these complexes the Dyall-TZ/IGLO-III basis set and the PBE0 functional may already be considered sufficient. However, larger deviations are observed for the Re complexes with 60 ppt for $[ReOBr_4]$ and about 80 ppt for $[ReOF_5]^-$. These are errors of about 60% for $[ReOBr_4]$ and 30% for $[ReOF_5]^-$.

23

Table 3: Principal components of the g-tensor relative to that of the free electron in ppt. Non-collinear 4c results are taken from the Supporting Information of Ref. 29. "PCC" denotes that the derivatives of $\boldsymbol{X}$ and $\boldsymbol{R}$ are neglected. Experimental (Expt.) results[211–222] were collected in Ref. 29. All calculations utilize a common gauge origin and the RKB condition. Results with the Sapporo-DKH3-QZP-2012-diffuse bases are listed in the Supporting Information.

Molecule	Hamiltonian	Δg_{iso}	$\Delta g_{\parallel}$	$\Delta g_{\perp}$	Molecule	Hamiltonian	Δg_{iso}	$\Delta g_{\parallel}$	$\Delta g_{\perp}$
$[\mathbf{MoNCl_4}]^{2-}$	X2C RKB PCC	−43.4	−88.9	−20.7	$[\mathbf{TcNF_4}]^{-}$	X2C RKB PCC	−41.5	−77.6	−23.4
	X2C RKB	−43.9	−89.5	−21.1		X2C RKB	−42.0	−78.3	−23.8
	DLU RKB PCC	−43.4	−88.9	−20.8		DLU RKB PCC	−41.5	−77.7	−23.4
	DLU RKB	−44.0	−89.5	−21.3		DLU RKB	−42.1	−78.4	−23.9
	4c RKB	−43	−90	−20		4c RKB	−41	−78	−23
	Expt.	−44	−96	−18		Expt.	−44	−107	−12
$[\mathbf{MoOF_4}]^{-}$	X2C RKB PCC	−75.9	−94.2	−66.8	$[\mathbf{TcNCl_4}]^{-}$	X2C RKB PCC	5.7	26.2	−4.6
	X2C RKB	−76.4	−94.8	−67.2		X2C RKB	5.2	25.5	−4.9
	DLU RKB PCC	−75.9	−94.1	−66.9		DLU RKB PCC	5.7	26.2	−4.5
	DLU RKB	−76.6	−94.9	−67.4		DLU RKB	5.2	25.6	−5.0
	4c RKB	−77	−96	−67		4c RKB	7	27	−3
	Expt.	−87	−108	−77		Expt.	0	6	−2
$[\mathbf{MoOCl_4}]^{-}$	X2C RKB PCC	−42.3	−16.9	−55.0	$[\mathbf{TcNBr_4}]^{-}$	X2C RKB PCC	79.6	178.4	30.1
	X2C RKB	−42.7	−17.5	−55.4		X2C RKB	79.0	177.7	29.7
	DLU RKB PCC	−42.4	−16.9	−55.1		DLU RKB PCC	79.6	178.5	30.2
	DLU RKB	−42.9	−17.6	−55.6		DLU RKB	78.9	177.6	29.5
	4c RKB	−42	−17	−55		4c RKB	81	180	31
	Expt.	−49	−37	−56		Expt.	69	145	32
$[\mathbf{MoOF_5}]^{2-}$	X2C RKB PCC	−104.5	−101.6	−105.9	$[\mathbf{ReNF_4}]^{-}$	X2C RKB PCC	−188.5	−329.0	−118.2
	X2C RKB	−104.9	−102.2	−106.3		X2C RKB	−189.2	−330.1	−118.8
	DLU RKB PCC	−104.5	−101.5	−105.9		DLU RKB PCC	−188.4	−328.8	−118.1
	DLU RKB	−105.1	−102.3	−106.5		DLU RKB	−189.4	−330.1	−119.0
	4c RKB	−106	−104	−108		4c RKB	−186	−326	−116
	Expt.	−104	−128	−91		Expt.	−206	−353	−132
$[\mathbf{MoOBr_5}]^{2-}$	X2C RKB PCC	−7.2	103.8	−62.7	$[\mathbf{ReNCl_4}]^{-}$	X2C RKB PCC	−75.2	−72.7	−76.4
	X2C RKB	−7.7	103.1	−63.1		X2C RKB	−76.0	−73.8	−77.0
	DLU RKB PCC	−7.4	103.7	−62.9		DLU RKB PCC	−75.1	−72.7	−76.3
	DLU RKB	−8.2	102.7	−63.7		DLU RKB	−75.9	−73.7	−77.0
	4c RKB	−7	104	−63		4c RKB	−74	−72	−74
	Expt.	−9	87	−57		Expt.	−78	−87	−73
$[\mathbf{WOCl_4}]^{-}$	X2C RKB PCC	−201.2	−180.8	−211.4	$[\mathbf{ReNBr_4}]^{-}$	X2C RKB PCC	10.1	109.3	−39.5
	X2C RKB	−201.9	−181.8	−212.0		X2C RKB	9.2	108.1	−40.2
	DLU RKB PCC	−201.1	−180.7	−211.3		DLU RKB PCC	10.2	109.3	−39.4
	DLU RKB	−201.9	−181.7	−211.9		DLU RKB	9.1	108.0	−40.4
	4c RKB	−198	−179	−208		4c RKB	11	109	−38
	Expt.	−229	−209	−239		Expt.	3	67	−29
$[\mathbf{WOF_5}]^{2-}$	X2C RKB PCC	−391.5	−455.8	−359.4	$[\mathbf{ReOBr_4}]$	X2C RKB PCC	−39.4	230.8	−174.5
	X2C RKB	−392.2	−456.9	−359.9		X2C RKB	−40.2	229.7	−175.2
	DLU RKB PCC	−391.4	−455.7	−359.3		DLU RKB PCC	−39.3	230.9	−174.4
	DLU RKB	−392.4	−457.0	−360.1		DLU RKB	−40.3	229.5	−175.3
	4c RKB	−388	−451	−356		4c RKB	−37	231	−172
	Expt.	−368	−443	−330		Expt.	−98	171	−232
$[\mathbf{WOBr_5}]^{2-}$	X2C RKB PCC	−190.3	−82.1	−244.5	$[\mathbf{ReOF_5}]^{-}$	X2C RKB PCC	−351.5	−317.8	−368.4
	X2C RKB	−191.1	−83.2	−245.1		X2C RKB	−352.3	−318.9	−369.0
	DLU RKB PCC	−190.3	−82.1	−244.4		DLU RKB PCC	−351.4	−317.6	−368.4
	DLU RKB	−191.5	−83.5	−245.4		DLU RKB	−352.4	−318.9	−369.2
	4c RKB	−187	−81	−240		4c RKB	−348	−314	−365
	Expt.	−172	−99	−206		Expt.	−269	−282	−262
$[\mathbf{OsOF_5}]$	X2C RKB PCC	−312.2	−182.7	−376.9					
	X2C RKB	−313.0	−183.8	−377.5					
	DLU RKB PCC	−312.1	−182.6	−376.9					
	DLU RKB	−313.1	−183.8	−377.7					
	4c RKB	−309	−180	−374					
	Expt.	−324	−197	−387					

Second, the error introduced by the DLU scheme is negligible. For the Mo and Tc complexes, the error is typically about 0.1 ppt. The maximum error is 0.4 ppt for the isotropic Δg shift of $[WOBr_5]^{2-}$, compared to an absolute value of 190 ppt. The errors of the principal components are very similar. Thus, no error cancellation is observed and the DLU scheme is a robust approximation. This confirms our previous findings for the HFC constant.[73]

Third, the impact of the decoupling derivatives typically amounts to about 1 ppt for the heavier compounds. This may validate the previous X2C implementation for the EPR g-tensor in Ref. 77. Notably, the error introduced by neglecting the decoupling derivatives is clearly larger than the error introduced by the local approximation and the derivatives can therefore routinely be included in DLU-X2C calculations with almost no computational overhead compared to a DLU-X2C energy calculation. For these complexes, the calculation of the g-tensor with the DLU-X2C Hamiltonian including derivatives takes a few seconds only. The computational costs are considered in detail in Sec. 6.4.

The three different approaches to the EPR g-tensor, i.e. RKB-CGO, RMB-CGO, and RMB-GIAO, are compared in Tab. 4. The DLU error is negligible in all cases, which further demonstrates the broad applicability of this approximation. Overall, the impact of the RMB and the GIAOs on the actual results is comparably small. As expected, the largest absolute deviations are found for the heavy W, Re, and Os compounds. There, deviations of about 2–3 ppt are observed. For $[ReNBr_4]^-$, this amounts to a relative change of about 17%, while it amounts to only 1% for $[ReOF_5]^-$. The small impact of the GIAOs can be rationalized by analyzing the individual terms for the EPR g-tensor in Eq. 28. The contribution of the one-electron potential and the two-electron integrals compensate each other to a large extent. The main advantage of GIAOs is that the working equations become gauge-origin invariant. The price to pay for this physical constraint is the evaluation of the two-electron integrals—especially the HF exchange integrals. For instance, the calculation of the g-tensor of $[OsOF_5]$ with 499 basis functions (spherical atomic orbital representation) takes about 8.8 minutes with the RMB-GIAO ansatz. Here, the computation of the one-electron terms requires 6

Table 4: Comparison of two-component Hamiltonians for the principal components of the Δg-tensor in ppt. Experimental (Expt.) results[211–222] were collected in Ref. 29.

Molecule	Hamiltonian	Δg_{iso}	$\Delta g_{\parallel}$	$\Delta g_{\perp}$	Molecule	Hamiltonian	Δg_{iso}	$\Delta g_{\parallel}$	$\Delta g_{\perp}$
$[MoNCl_4]^{2-}$	X2C RKB	−43.9	−89.5	−21.1	$[TcNF_4]^-$	X2C RKB	−42.0	−78.3	−23.8
	X2C RMB	−43.2	−88.8	−20.4		X2C RMB	−41.2	−77.5	−23.1
	X2C GIAO	−42.4	−88.0	−19.7		X2C GIAO	−40.8	−76.6	−22.9
	DLU RKB	−44.0	−89.5	−21.3		DLU RKB	−42.1	−78.4	−23.9
	DLU RMB	−43.2	−88.8	−20.5		DLU RMB	−41.3	−77.6	−23.1
	DLU GIAO	−42.5	−88.0	−19.8		DLU GIAO	−40.9	−76.8	−22.9
	Expt.	−44	−96	−18		Expt.	−44	−107	−12
$[MoOF_4]^-$	X2C RKB	−76.4	−94.8	−67.2	$[TcNCl_4]^-$	X2C RKB	5.2	25.5	−4.9
	X2C RMB	−75.7	−94.0	−66.5		X2C RMB	5.9	26.3	−4.2
	X2C GIAO	−75.2	−93.3	−66.1		X2C GIAO	6.5	27.4	−3.9
	DLU RKB	−76.6	−94.9	−67.4		DLU RKB	5.2	25.6	−5.0
	DLU RMB	−75.7	−94.0	−66.6		DLU RMB	5.9	26.2	−4.2
	DLU GIAO	−75.2	−93.4	−66.2		DLU GIAO	6.5	27.4	−3.9
	Expt.	−87	−108	−77		Expt.	0	6	−2
$[MoOCl_4]^-$	X2C RKB	−42.7	−17.5	−55.4	$[TcNBr_4]^-$	X2C RKB	79.0	177.7	29.7
	X2C RMB	−42.0	−16.8	−54.7		X2C RMB	79.9	178.6	30.6
	X2C GIAO	−41.4	−15.9	−54.2		X2C GIAO	80.6	179.3	31.3
	DLU RKB	−42.9	−17.6	−55.6		DLU RKB	78.9	177.6	29.5
	DLU RMB	−42.1	−16.8	−54.8		DLU RMB	79.9	178.6	30.6
	DLU GIAO	−41.5	−15.9	−54.3		DLU GIAO	80.6	179.3	31.2
	Expt.	−49	−37	−56		Expt.	69	145	32
$[MoOF_5]^{2-}$	X2C RKB	−104.9	−102.2	−106.3	$[ReNF_4]^-$	X2C RKB	−189.2	−330.1	−118.8
	X2C RMB	−104.2	−101.4	−105.5		X2C RM	−188.7	−329.5	−118.3
	X2C GIAO	−103.4	−100.5	−104.9		X2C GIAO	−187.2	−326.5	−117.5
	DLU RKB	−105.1	−102.3	−106.5		DLU RKB	−189.4	−330.1	−119.0
	DLU RMB	−104.2	−101.4	−105.6		DLU RMB	−188.7	−329.5	−118.3
	DLU GIAO	−103.5	−100.6	−104.9		DLU GIAO	−187.2	−326.5	−117.5
	Expt.	−104	−128	−91		Expt.	−206	−353	−132
$[MoOBr_5]^{2-}$	X2C RKB	−7.7	103.1	−63.1	$[ReNCl_4]^-$	X2C RKB	−76.0	−73.8	−77.0
	X2C RMB	−6.7	104.1	−62.1		X2C RMB	−75.5	−73.3	−76.6
	X2C GIAO	−6.5	104.7	−62.1		X2C GIAO	−74.5	−72.2	−75.6
	DLU RKB	−8.2	102.7	−63.7		DLU RKB	−75.9	−73.7	−77.0
	DLU RMB	−7.0	104.0	−62.4		DLU RMB	−75.5	−73.4	−76.6
	DLU GIAO	−6.7	104.6	−62.4		DLU GIAO	−74.4	−72.2	−75.6
	Expt.	−9	87	−57		Expt.	−78	−87	−73
$[WOCl_4]^-$	X2C RKB	−201.9	−181.8	−212.0	$[ReNBr_4]^-$	X2C RKB	9.2	108.1	−40.2
	X2C RMB	−201.4	−181.3	−211.5		X2C RMB	9.8	108.7	−39.7
	X2C GIAO	−200.6	−180.4	−210.6		X2C GIAO	10.8	110.7	−39.1
	DLU RKB	−201.9	−181.7	−211.9		DLU RKB	9.1	108.0	−40.4
	DLU RMB	−201.4	−181.3	−211.5		DLU RMB	9.8	108.6	−39.6
	DLU GIAO	−200.5	−180.4	−210.6		DLU GIAO	10.8	110.7	−39.1
	Expt.	−229	−209	−239		Expt.	3	67	−29
$[WOF_5]^{2-}$	X2C RKB	−392.2	−456.9	−359.9	$[ReOBr_4]$	X2C RKB	−40.2	229.7	−175.2
	X2C RMB	−391.7	−456.3	−359.4		X2C RMB	−39.7	230.3	−174.6
	X2C GIAO	−389.2	−451.8	−358.0		X2C GIAO	−39.3	230.7	−174.2
	DLU RKB	−392.4	−457.0	−360.2		DLU RKB	−40.3	229.5	−175.3
	DLU RMB	−391.8	−456.4	−359.4		DLU RMB	−39.7	230.2	−174.6
	DLU GIAO	−389.3	−451.8	−358.0		DLU GIAO	−39.2	230.7	−174.2
	Expt.	−368	−443	−330		Expt.	−98	171	−232
$[WOBr_5]^{2-}$	X2C RKB	−191.1	−83.2	−245.1	$[ReOF_5]^-$	X2C RKB	−352.3	−318.9	−369.0
	X2C RMB	−190.5	−82.6	−244.5		X2C RMB	−351.7	−318.3	−368.5
	X2C GIAO	−190.1	−79.3	−245.5		X2C GIAO	−350.3	−315.1	−367.8
	DLU RKB	−191.5	−83.5	−245.4		DLU RKB	−352.4	−318.9	−369.2
	DLU RMB	−190.6	−82.7	−244.5		DLU RMB	−351.8	−318.3	−368.5
	DLU GIAO	−190.1	−79.3	−245.5		DLU GIAO	−350.3	−315.1	−367.8
	Expt.	−172	−99	−206		Expt.	−269	−282	−262
$[OsOF_5]$	X2C RKB	−313.0	−183.8	−377.5					
	X2C RMB	−312.4	−183.3	−376.9					
	X2C GIAO	−311.8	−181.7	−376.8					
	DLU RKB	−313.1	−183.8	−377.7					
	DLU RMB	−312.4	−183.2	−376.9					
	DLU GIAO	−311.8	−181.7	−376.8					
	Expt.	−324	−197	−387					

seconds. In contrast, only 4 and 5 seconds are required for the RKB-CGO and RMB-CGO approach, respectively. Timings are measured with the DLU-X2C Hamiltonian and a single thread of an Intel® Xeon® Gold 6212U CPU @ 2.40 GHz. For this purpose, the code was compiled with Intel® Fortran Compiler 19.0.1.144. Compared to the SCF procedure, this computational effort is negligible with all approaches for the g-tensor.
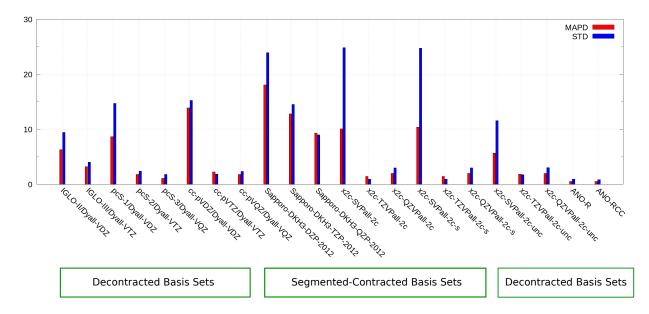
6.2   Basis Set Study

The results of the relativistic all-electron basis set study on the 15 aforementioned transition-metal complexes are summarized in Figure 1. For each basis set, the mean absolute percent-wise deviation (MAPD) and the corresponding standard deviation (STD) were computed over the sum of the 15 compounds. The MAPD is calculated as follows:

$$\text{MAPD} = \sum_{i=1}^{N=15} \frac{|\Delta g_{i,\text{iso}}^{\text{test}} - \Delta g_{i,\text{iso}}^{\text{ref}}|}{|\Delta g_{i,\text{iso}}^{\text{ref}}|} \tag{57}$$

where $\Delta g_{i,\text{iso}}^{\text{test}}$ and $\Delta g_{i,\text{iso}}^{\text{ref}}$ denote the isotropic g-shift for the test basis set and the reference basis set, respectively.

From the figure, it is clear that the Sapporo-type basis sets perform consistently worse than the others included in this study, which starkly contrasts with its good performance for the HFC constant observed in our previous work for the same set of compounds.[73] Even the quadruple-ζ analog of the Sapporo basis sets results in an MAPD and STD of over 9.32%, which is far larger than that of the pcS-3/Dyall-VQZ (1.10%), cc-pVQZ/Dyall-VQZ (1.80%), and x2c-QZVPall-2c (1.98%) configurations. Thus, the results are more similar to the NMR shielding studies, in which the x2c-type and Dyall bases also outperformed the Sapporo basis sets.[164,176]

Conversely, the triple-ζ quality basis sets aside from the Sapporo-DKH3-TZP-2012 configurations achieve accurate results when compared to the reference values, with MAPDs of less than 3%. In particular, going to the quadrupole-ζ quality analog did not significantly

Figure 1: Assessment of various basis sets compared to an even-tempered reference for 15 of the 17 transition-metal complexes. $[TcNCl_4]^-$ is omitted due to a small absolute Δg shift (4 ppt) and $[WOF_5]^{2-}$ is neglected in the statistical evaluation due to convergence issues for the alignment of spin x and y with the ET basis. MAPD and STD denote the mean absolute percent-wise error and its standard deviation. For brevity, the suffix "unc" is omitted for the combinations of the Dyall basis and the ANO basis sets. See Tab. 1 for further details on the basis sets and their size. Note that we excluded the Jorge basis sets due to large errors of more than 90%.

change the MAPD and STD for all basis sets. This also holds true when comparing the de-contracted and contracted x2c-XZVPall-2c (X=T,Q) basis sets. The ANO-R and ANO-RCC basis sets achieve the lowest MAPD and STD of all configurations studied, at 0.52/0.94 and 0.53/0.87, respectively.

In summary, these results indicate that triple-ζ quality basis sets are sufficient for accurate calculations of the g-tensor when using the cc-pVTZ/Dyall-VTZ, x2c-TZVPall-2c, and x2c-TZVPall-2c-s basis sets for these species. In particular, quadrupole-ζ or even decontracted basis sets are unnecessary if the x2c-TZVPall-2c basis set is used, which significantly reduces the total basis set dimension (see also Tab. 1). The quadruple-ζ basis sets may be used for benchmark calculations.
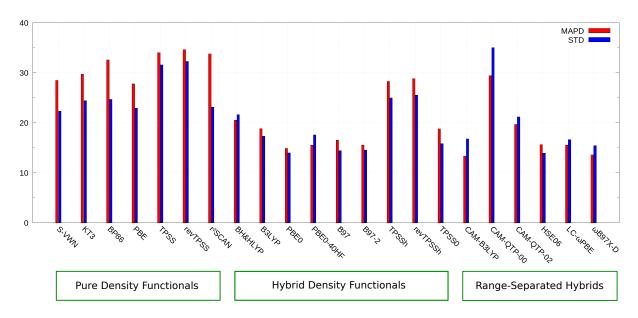
6.3 Study of Density Functional Approximations

The impact of frequently used density functionals of various rungs is shown in Fig. 2 for the set of 17 transition–metal complexes. Similar to other magnetic properties,[125,227–234] hybrid functionals usually lead to an improvement over pure density functionals. Yet, the errors of the hybrid functionals are systematically larger than those found previously for the EPR HFC constant. Specifically, the errors for the g-tensor range from roughly 10% to less than 30%, whereas errors for the HFC constant span from 5% to less than 25%.[73]

Considering the Laplacian or the (generalized) kinetic energy in the functional approximation does not reduce the errors. Here, we observe just the opposite, and the performance of all *meta*-GGAs is notably inferior to that of GGAs. Particularly, the performance of r^{2}SCAN deteriorates substantially, in contrast to the considerable improvement over GGAs that r^{2}SCAN gave for HFC constants.[73]

The errors of GGA hybrid functionals cover a range from 15% to 20%. The B97 family and PBE0 perform best within this class. Note that B97 and B3LYP performed poorly

Figure 2: Assessment of density functional approximations compared to the experimental findings for 15 of the 17 transition-metal complexes. [ReNBr$_4$]$^-$ and [TcNCl$_4$]$^-$ are neglected in the statistical evaluation. MAPD and STD denote the mean absolute percent-wise error and its standard deviation.

for the HFC constants. TPSSh and revTPSSh do not include a sufficient amount of HF exchange as shown by the reduced errors of TPSS0 with 25% of exchange instead of 10%. The performance of the latter is on par with B3LYP and BH&HLYP. Range-separation or the Coulomb attenuating method do not achieve consistent improvements; whereas CAM-B3LYP reduced the errors compared to its parent B3LYP, CAM-QTP-00 shows the largest errors among all hybrid functionals. PBE0, LC-ωPBE, and ωB97X-D show very similar errors as for the HFC constant. The MAPDs amount to about 15% and we recommend these functionals for an error-balanced calculation of EPR spectra.

6.4   Application to $[Pt(C_6Cl_5)_4]^-$

To illustrate the computational costs, we apply the X2C and the DLU-X2C Hamiltonian to $[Pt(C_6Cl_5)_4]^-$, described by more than 3000 basis functions. The Δg shifts are listed in Tab. 5. In line with the previous study of the density functional approximations, we only consider hybrid density functionals.

Generally, the uncontracted Dyall-VTZ/pcS-2 and the segmented-contracted x2c-QZVPall-2c basis sets lead to very similar results with the RKB and RMB condition using a common gauge origin as well as the RMB-GIAO ansatz. Notably, the magnetic-field derivatives of COSMO do not lead to substantial changes. We note that an improved relativistic description with COSMO formally requires further generalizations in two aspects. First, the parameters such as the solvation radii and the grids for the COSMO surface are not optimized for relativistic all-electron calculations.[146,147] Second, we do not apply the relativistic picture-change correction to COSMO. Such a correction is less straightforward to implement than the corresponding correction to expectation values since the COSMO surface is optimized in the SCF iterations.[146,147]

Overall, the CAM-QTP functionals perform remarkably well for the isotropic shift and the three principal components. Note that this performance of CAM-QTP-00 is in stark contrast to the findings in Sec. 6.3 and the accuracy of CAM-QTP-00 significantly depends

Table 5: Principal components of the Δg shift for $[Pt(C_6Cl_5)_4]^-$ in ppt. RKB and RMB refer to restricted kinetic and magnetic balance, while CGO and GIAO denote a common gauge origin and gauge-including atomic orbitals, respectively. We use the mSNSO-DLU-X2C Hamiltonian. Experimental (Expt.) results are taken from Ref. 235.

Functional	Hamiltonian	Dyall-VTZ-unc/pcS-2-unc				x2c-QZVPall-2c			
		Δg_{iso}	Δg_{11}	Δg_{22}	Δg_{33}	Δg_{iso}	Δg_{11}	Δg_{22}	Δg_{33}
BH&HLYP	RKB CGO	553	−372	953	1078	549	−374	949	1072
	RMB CGO	554	−371	954	1079	550	−372	950	1072
	RMB GIAO	553	−371	953	1079	550	−372	950	1072
B3LYP	RKB CGO	425	−409	648	1002	420	−412	676	997
	RMB CGO	427	−408	685	1003	422	−410	678	998
	RMB GIAO	426	−408	683	1004	422	−410	678	998
PBE0	RKB CGO	462	−350	787	948	454	−354	779	938
	RMB CGO	463	−349	788	949	456	−352	780	939
	RMB GIAO	462	−349	787	949	456	−352	780	939
PBE0-40HF	RKB CGO	513	−337	888	988	510	−341	885	986
	RMB CGO	514	−337	890	989	511	−339	886	987
	RMB GIAO	513	−337	888	989	511	−339	886	987
TPSSh	RKB CGO	326	−355	581	751	317	−359	576	734
	RMB CGO	327	−354	582	752	319	−357	578	736
	RMB GIAO	333	−351	588	762	325	−354	585	745
TPSS0	RKB CGO	435	−310	752	864	430	−313	747	856
	RMB CGO	436	−309	753	865	430	−313	747	856
	RMB GIAO	441	−307	759	873	437	−310	755	865
CAM-B3LYP	RKB CGO	535	−397	919	1083	534	−399	917	1084
	RMB CGO	536	−396	921	1084	535	−398	918	1085
	RMB GIAO	536	−396	919	1084	535	−398	918	1085
CAM-QTP-00	RKB CGO	601	−382	1034	1150	603	−384	1035	1158
	RMB CGO	602	−381	1036	1151	604	−382	1036	1158
	RMB GIAO	601	−381	1034	1150	604	−382	1036	1158
CAM-QTP-02	RKB CGO	614	−413	1057	1198	609	−416	1056	1186
	RMB CGO	615	−413	1058	1199	610	−415	1057	1187
	RMB GIAO	614	−413	1056	1198	610	−415	1057	1187
HSE06	RKB CGO	446	−364	759	943	443	−367	754	941
	RMB CGO	447	−363	760	945	444	−365	755	942
	RMB GIAO	447	−363	758	945	444	−365	755	943
LC-ωPBE	RKB CGO	534	−349	940	1011	531	−353	938	1008
	RMB CGO	535	−348	942	1012	532	−351	939	1008
	RMB GIAO	534	−348	940	1011	532	−351	939	1009
ωB97X-D	RKB CGO	529	−398	893	1093	528	−401	891	1094
	RMB CGO	530	−397	894	1094	529	−399	892	1095
	RMB GIAO	530	−397	893	1094	529	−399	892	1095
Expt.		594	−400	1005	1177	594	−400	1005	1177

on the molecule. ωB97X-D reproduces one of the three components very well but loses some ground for the other components. Generally, range-separated functionals and Becke's half and half functional (BH&HLYP) yield the most accurate results for this complex. This is in line with previous studies on the HFC constant[29,73] and also similar to results for other magnetic properties.[125,227–234] TPSSh and HSE06 are not sufficient as they fail to deliver accurate results for Δg_{22} and Δg_{33}. Again, this may be explained by the fact that TPSSh only includes 10% of HF exchange. Consequently, TPSS0 significantly improves upon TPSSh. Moreover, we previously observed that the results with HSE06 deteriorate for the HFC tensor of larger molecules.[73]

We discuss the computational costs for the PBE0 functional. First, a two-component SCF calculation with the uncontracted Dyall-VTZ/pcS-2 basis set (3360 basis functions in the spherical representation) takes between 5.5 and 8 hours on 12 threads of an Intel® Xeon® Gold 6212U CPU @ 2.40 GHz. This requires 69–109 iterations. The calculation of the g-tensor with a common gauge origin only takes 17 seconds with the DLU scheme and the RKB condition. This is increased to 22 seconds with the RMB condition. The RMB-GIAO approach requires 1.0 hours. Here, the one-electron terms need 47 seconds, while the computation of the Coulomb and the HF exchange integrals amounts to 57.5 minutes. The derivatives of the exchange-correlation energy are evaluated in 2 minutes. Thus, efficient and robust approximations to the HF exchange integrals such as an extension of the two-component seminumerical exchange approximation for SCF energies[130,131] to magnetic-field derivatives are desirable. Matters are similar for the x2c-QZVPall-2c basis set, which leads to 3003 basis functions in total (4720 primitive basis functions). Here, the SCF procedure requires 26.5 to 41.9 hours for 64–106 SCF iterations, see also Ref. 73. The RKB-CGO and RMB-CGO calculations of the g-tensor take 1.0 and 1.5 minutes, respectively. This is increased to 4.2 hours with the RMB-GIAO ansatz, for which the one-electron parts need 2.7 minutes and the two-electron integrals require the remaining 98% of the computational time (4.1 hours). The RI-J and the XC terms only take 2.5 and 7.1 minutes, respectively.

Again, the HF exchange integrals dominate the computational costs for this approach. The acceleration of the DLU scheme is significant as the formal scaling of the one-electron Hamiltonian (derivatives) is reduced form $\mathcal{O}(N^3)$ to $\mathcal{O}(N^2)$, where N measures the system-size. For the RKB-CGO and the RMB-CGO approach, the full X2C Hamiltonian needs 64.8 and 69.7 minutes, whereas the wall time for RMB-GIAO is 75 minutes. Therefore, the DLU scheme leads to a speed-up by a factor of 29–61 for the one-electron part and the maximum error for the principle components amounts to about 5 ppt for both x2c-QZVPall-2c and the Dyall bases. The errors of isotropic the Δg shift are 1.5 ppt and 2.2 ppt. The speed-up decreases from RKB-CGO to RMB-GIAO as more integral derivatives need to be evaluated and all blocks of the integrals are required for the DLU scheme to consider the interatomic off-diagonal corrections. For pure density functionals, the computation time of the full X2C Hamiltonian is much larger than that of the RI-J integrals and the XC terms. Therefore, the X2C step will dominate the corresponding computational costs for pure density functionals.

In conclusion, calculations of large molecules are possible with limited computational resources and the convergence of the SCF procedure is the time-determining part of the computational protocol. Therefore, the GIAO-RMB ansatz can be routinely used for large-scale calculations.

7   Application to Lanthanide Molecules

We recently demonstrated that our implementation of the hyperfine coupling constant within the one-electron exact two-component theory framework accurately reproduces the experimental HFC constants of the three lanthanide complexes $[La(OAr^*)_3]^-$, $[Lu(NR_2)_3]^-$, and $[Lu(OAr^*)_3]^-$ of Ref. 8, which represent potential molecular qubit materials.[73]

To supplement this study and demonstrate that the spin Hamiltonian parameters for this class of important compounds can be accurately predicted by the present method, we calculate the g-tensors for the experimental HFC constants of the three lanthanide complexes

Table 6: Principal components of the g-tensor for the three spin-$\frac{1}{2}$ La(II) and Lu(II) molecules [La(OAr*)$_3$]$^-$, Lu(NR$_2$)$_3$]$^-$, and [Lu(OAr*)$_3$]$^-$ (OAr* = 2,6-Ad$_2$-4-t-Bu-C$_6$H$_2$O, Ad = adamantyl, t-Bu= tert-butyl, R = SiMe$_3$ with Me = methyl).[8] RKB and RMB refer to restricted kinetic and magnetic balance, while CGO and GIAO denote a common gauge origin and gauge-including atomic orbitals, respectively. We use the mSNSO-DLU-X2C Hamiltonian. The x2c-TZVPPall-2c/x2c-SVPall-2c basis sets are employed. We refer to the Supporting Information with the results obtained using the x2c-QZVPall-2c/x2c-SVPall-2c basis sets. Experimental (Expt.) results are taken from Ref. 8. Th experimental uncertainties are 0.002.

Functional	Hamiltonian	[La(OAr*)$_3$]$^-$			[Lu(NR$_2$)$_3$]$^-$			[Lu(OAr*)$_3$]$^-$		
		g_{11}	g_{22}	g_{33}	g_{11}	g_{22}	g_{33}	g_{11}	g_{22}	g_{33}
TPSS	RKB CGO	1.897	1.897	1.998	1.885	1.885	1.995	1.907	1.907	1.995
	RMB CGO	1.897	1.897	1.998	1.886	1.886	1.996	1.909	1.909	1.998
	RMB GIAO	1.895	1.895	1.998	1.884	1.884	1.997	1.909	1.909	1.998
r^{2}SCAN	RKB CGO	1.905	1.905	1.996	1.890	1.890	1.996	1.908	1.908	1.996
	RMB CGO	1.907	1.908	1.998	1.891	1.891	1.998	1.911	1.911	1.998
	RMB GIAO	1.902	1.903	1.998	1.887	1.887	1.998	1.908	1.908	1.999
PBE0	RKB CGO	1.886	1.886	1.995	1.886	1.886	1.996	1.906	1.906	1.996
	RMB CGO	1.888	1.888	1.997	1.887	1.887	1.997	1.909	1.909	1.998
	RMB GIAO	1.888	1.888	1.997	1.887	1.887	1.997	1.909	1.909	1.998
PBE0-40HF	RKB CGO	1.893	1.894	1.997	1.891	1.891	1.996	1.912	1.917	1.997
	RMB CGO	1.895	1.896	1.998	1.892	1.892	1.998	1.915	1.920	1.999
	RMB GIAO	1.894	1.895	1.998	1.892	1.892	1.998	1.914	1.919	1.999
CAM-QTP-02	RKB CGO	1.890	1.892	1.997	1.878	1.878	1.996	1.900	1.901	1.996
	RMB CGO	1.892	1.894	1.999	1.879	1.879	1.998	1.903	1.904	1.999
	RMB GIAO	1.891	1.893	1.999	1.879	1.879	1.998	1.902	1.903	1.999
HSE06	RKB CGO	1.914	1.916	1.998	1.889	1.889	1.996	1.917	1.918	1.997
	RMB CGO	1.916	1.918	1.999	1.890	1.890	1.998	1.919	1.921	1.999
	RMB GIAO	1.913	1.915	1.999	1.890	1.890	1.998	1.917	1.919	1.999
ωB97X-D	RKB CGO	1.879	1.880	1.996	1.875	1.877	1.996	1.900	1.901	1.996
	RMB CGO	1.881	1.882	1.997	1.876	1.879	1.998	1.903	1.904	1.998
	RMB GIAO	1.879	1.881	1.997	1.876	1.878	1.998	1.902	1.903	1.998
Expt.		1.876	1.886	2.000	1.882	1.898	2.000	1.915	1.915	2.000

[La(OAr*)$_3$]$^-$, [Lu(NR$_2$)$_3$]$^-$, and [Lu(OAr*)$_3$]$^-$ using the RKB-CGO, RMB-CGO, and RMB-GIAO approaches for a selection of density functionals evaluated in Section 6.3. Results obtained using the x2c-TZVPPall-2c/x2c-SVPall-2c basis set combination are provided in Table 6, whereas the results using the x2c-QZVPall-2c/x2c-SVPall-2c basis sets are given as Supporting Information.

While in some cases the RMB GIAO ansatz yielded modest improvements to the predicted g-tensor components in [La(OAr*)$_3$]$^-$, [Lu(NR$_2$)$_3$]$^-$, and [Lu(OAr*)$_3$]$^-$, the overall differences

between the three ansätze remained small, as observed in previous results reported above. In the following discussion, we therefore compare RMB GIAO results with experimental results, and errors in g-tensor components are computed as shifts in ppt by: $\Delta g = (g - g_{\text{expt}}) \cdot 1000$.

$[La(OAr^*)_3]^-$ appeared to be a particularly difficult case for the majority of the density functionals tested, with errors in g_{11} exceeding 15 ppt for all functionals but ωB97X-D and PBE0. In particular, HSE06 performed the worst for $[La(OAr^*)_3]^-$ with errors in g_{11} and g_{22} of approximately 37 ppt and 19 ppt, respectively, exceeding those of both r²SCAN and TPSS. The performance of all functionals were more consistent between themselves for complex $[Lu(NR_2)_3]^-$, with errors less than 20 ppt for all principal components of the g-tensor. The g_{22} component gave rise to the largest errors, which were universally underestimated by all functionals but worst captured by ωB97X-D and CAM-QTP-02, giving 19 ppt error in each case. For compound $[Lu(OAr^*)_3]^-$, the ωB97X-D and CAM-QTP-02 functionals again performed the worst for g_{11} and g_{22} with errors of over 12 ppt. In contrast, the hybrids and pure functionals performed well with errors of less than 8 ppt for both components. Surprisingly, HSE06 yielded the most accurate g-tensor for this compound, despite the fact that it performed the worst for $[La(OAr^*)_3]^-$. These observations also hold for predictions of the g-tensor obtained using the x2c-QZVPall-2c/x2c-SVPall-2c basis sets, which is included in the Supporting Information. This confirms the findings of Sec. 6.2 and shows that triple-ζ basis sets are sufficient for the calculation of the g-tensor.

The results indicate that accurate g-tensors for the three Ln compounds can be obtained using local exact two-component theory. Errors in the principal components of the g-tensor do not exceed 40 ppt for all functionals tested. However, due to the inconsistent accuracy of the range-separated hybrids between $[La(OAr^*)_3]^-$, $[Lu(NR_2)_3]^-$, and $[Lu(OAr^*)_3]^-$, hybrid functionals may be better suited for general application to these types of complexes.

8 Conclusions

A gauge-origin invariant formulation of exact two-component (X2C) theory for EPR g-tensors has been presented. This includes the complete derivative of the X2C Hamiltonian in the presence of an external magnetic field. Gauge-including atomic orbitals (GIAOs) and the restricted magnetic balance (RMB) condition are applied for the basis set expansion of the Dirac–Hamilton operator. Our implementation supports the finite nucleus model throughout, is fully integral direct, and parallelized using OpenMP. Furthermore, we apply the diagonal local approximation to the unitary decoupling transformation (DLU) to further reduce the computational costs. Together with our previously presented implementation of the EPR hyperfine coupling (HFC) constant,[73] routine calculations are now possible for large molecules with several thousand basis functions.

Explicit comparisons between the four-component Dirac–Kohn–Sham (DKS) approach and X2C/DLU-X2C show that the two-component ansatz accurately reproduces the results of the "fully" relativistic theory when accounting for the two-electron picture-change error with the modified screened nuclear spin–orbit (mSNSO) approximation. The error introduced by DLU is negligible and considerably smaller than the error introduced by neglecting the decoupling derivatives as done in previous implementations.[77] We assess the importance of GIAOs and the RMB condition for transition-metal complexes and lanthanide compounds. Here, the impact is found to be rather small for complexes consisting of one metal center, where the position of the common gauge origin is straightforward. The computational effort is dominated by the self-consistent field (SCF) procedure. Therefore, the gauge-invariant ansatz does not notably increase the computational costs as demonstrated for $[\text{Pt}(\text{C}_6\text{Cl}_5)_4]^-$ with more than 3000 basis functions.

In addition, we carry out extensive benchmark studies with 24 basis sets and 22 density functional approximations. This complements our previous study for the HFC constant[73] and reveals some notable differences for a computational treatment of the EPR g-tensor and HFC constant. For the g-tensor, triple-ζ basis sets such as the Sapporo, Dyall, or the Karlsruhe

x2c-type bases are generally sufficient, whereas the HFC constant requires larger basis sets or even fully decontracted bases. Therefore, we recommend the uncontracted Dyall-VTZ or segmented-contracted x2c-QZVPall-2c basis set for an error-balanced description of the two EPR parameters. This is especially important for relativistic calculations of the pseudo-contact shift for paramagnetic NMR spectra as this term consists of both the g-tensor and the HFC tensor.

Hybrid density functional approximations are required for accurate results. Compared to the HFC constant, a smaller amount of HF exchange is advantageous as evident from the performance of PBE0 and its modification with 40% of Harteee–Fock (HF) exchange. TPSSh and revTPSSh (10% HF exchange) are not sufficient, whereas TPSS0 (25% HF exchange) delivers good results. Thus, functionals with around 25% of HF exchange are a reasonable choice for the g-tensor. Range-separated hybrids are not a consistent improvement over conventional global hybrid functionals. CAM-B3LYP and ωB97-X perform best for the set of 17 transition-metal complexes, whereas CAM-QTP-00 leads to comparably large errors. The performance of the latter significantly depends on the molecular system, e.g., CAM-QTP-00 is among the top performers for the larger complex $[\mathrm{Pt}(\mathrm{C_6Cl_5})_4]^-$. Overall, PBE0, LC-$\omega$PBE, and ωB97-X yield similar errors for the g-tensor and the HFC tensor.

Finally, the applicability of our implementation is demonstrated for the three spin-(1/2) lanthanide compounds $[\mathrm{La}(\mathrm{OAr}^*)_3]^-$, $[\mathrm{Lu}(\mathrm{NR_2})_3]^-$, and $[\mathrm{Lu}(\mathrm{OAr}^*)_3]^-$, whose magnetic properties suggest design principles for engineering qubits using molecular spins. The principal components of the g-tensor reproduce experimental results well using x2c-TZVPPall-2c basis sets for the Ln atom and x2c-SVPall-2c basis sets for the ligand atoms. Unlike for the hyperfine coupling constant, the accuracy of range-separated hybrid functionals was inconsistent between the three Ln complexes, and thus hybrid functionals appear to provide more balanced accuracy for Ln species.

A Appendix

A.1 Simplification with Common Gauge Origin

Without GIAOs, no derivatives of the two-electron integrals will arise and the g-tensor reduces to

$$\frac{\mathrm{d}E}{\mathrm{d}B_u} = \mathrm{tr}\left[\boldsymbol{P}\left(\vec{J}_v\right) \boldsymbol{h}_u^B \right] \tag{58}$$

Note that we use the generalized kinetic energy density[152] for *meta*-generalized gradient approximations only with the GIAO-based approach. Thus, only the derivative of the one-electron Hamiltonian is required and this derivative is directly contracted with the SCF density matrix as done for the hyperfine coupling tensor.[73,75–77] Neglecting GIAOs in the relativistic 4c basis set expansion leads to[79]

$$\left|\psi_i^L\right\rangle = \sum_\mu c_{\mu i}^L \left|\phi_\mu\right\rangle \tag{59}$$

$$\left|\psi_i^S\right\rangle = \sum_\mu c_{\mu i}^S \frac{1}{2c}\vec{\sigma}\cdot\left(\hat{\vec{p}} + \frac{1}{c}\hat{\vec{\mathcal{A}}}_O\right)\left|\phi_\mu\right\rangle \tag{60}$$

where O refers to the common gauge origin (CGO), which is usually placed at the center of the heaviest atom or the center of mass. Then, the overlap matrix $\boldsymbol{S}$ and the potential matrix $\boldsymbol{V}$ are given by

$$\boldsymbol{S} = \begin{pmatrix} \mathbf{S} & 0 \\ 0 & \mathbf{S} \end{pmatrix}, \mathbf{S}_{\mu\nu} = \langle\lambda_\mu|\lambda_\nu\rangle \tag{61}$$

$$\boldsymbol{V} = \begin{pmatrix} \mathbf{V} & 0 \\ 0 & \mathbf{V} \end{pmatrix}, \mathbf{V}_{\mu\nu} = \langle\lambda_\mu|\hat{V}|\lambda_\nu\rangle \tag{62}$$

All other matrices are still not block-diagonal and read

$$\boldsymbol{\Pi}_{\mu\nu}^\dagger = \frac{1}{2}\langle\phi_\mu|\left[\vec{\sigma}\cdot(\hat{\vec{p}} + \frac{1}{c}\hat{\vec{\mathcal{A}}}_O)\right]\left[\vec{\sigma}\cdot(\hat{\vec{p}} + \frac{1}{c}\hat{\vec{\mathcal{A}}}_O)\right]|\phi_\nu\rangle \tag{63}$$

$$\boldsymbol{\Pi}_{\mu\nu} = \frac{1}{2}\langle\phi_\mu|[\vec{\sigma}\cdot(\hat{\vec{p}}+\frac{1}{c}\hat{\vec{\mathcal{A}}}_O)]\ [\vec{\sigma}\cdot(\hat{\vec{p}}+\frac{1}{c}\hat{\vec{\mathcal{A}}}_O)]|\phi_\nu\rangle \tag{64}$$

$$\boldsymbol{W}_{\mu\nu} = \langle\phi_\mu|[\vec{\sigma}\cdot(\hat{\vec{p}}+\frac{1}{c}\hat{\vec{\mathcal{A}}}_O)]\hat{V}[\vec{\sigma}\cdot(\hat{\vec{p}}+\frac{1}{c}\hat{\vec{\mathcal{A}}}_O)]|\phi_\nu\rangle, \tag{65}$$

$$\boldsymbol{T}_{\mu\nu} = \frac{1}{2}\langle\phi_\mu|[\vec{\sigma}\cdot(\hat{\vec{p}}+\frac{1}{c}\hat{\vec{\mathcal{A}}}_O)]\ [\vec{\sigma}\cdot(\hat{\vec{p}}+\frac{1}{c}\hat{\vec{\mathcal{A}}}_O)]|\phi_\nu\rangle \tag{66}$$

All matrices are Hermitian. Note that the derivatives of the overlap and the potential matrix with respect to the magnetic field will be zero. So, the response equations of Sec. 2.4 are simplified. The derivatives of $\boldsymbol{T}$, $\boldsymbol{\Pi}$, and $\boldsymbol{W}$ are still non-zero and given by

$$\left(\frac{\partial\boldsymbol{T}_{\mu\nu}}{\partial B_u}\right)_0 = \frac{1}{2c}\sigma_0\langle\lambda_\mu|(\hat{\vec{r}}_O\times\hat{\vec{p}})_u|\lambda_\nu\rangle + \frac{1}{2c}\sigma_u\langle\lambda_\mu|\lambda_\nu\rangle \tag{67}$$

$$\left(\frac{\partial\boldsymbol{\Pi}_{\mu\nu}^\dagger}{\partial B_u}\right)_0 = \frac{1}{2c}\sigma_0\langle\lambda_\mu|(\hat{\vec{r}}_O\times\hat{\vec{p}})_u|\lambda_\nu\rangle + \frac{1}{2c}\sigma_u\langle\lambda_\mu|\lambda_\nu\rangle \tag{68}$$

$$\begin{aligned}\left(\frac{\partial\boldsymbol{W}_{\mu\nu}}{\partial B_u}\right)_0 = \ &+\frac{1}{2c}\sigma_0\langle\lambda_\mu|(\hat{\vec{r}}_O\times\hat{\vec{p}})_u\,\hat{V} + \hat{V}\,(\hat{\vec{r}}_O\times\hat{\vec{p}})_u|\lambda_\nu\rangle \\ &+\langle\lambda_\mu|\frac{i}{2c}\sigma_u\left(\hat{\vec{p}}\,\hat{V}\right)\cdot\hat{\vec{r}}_O - \frac{i}{2c}\left(\hat{\vec{p}}\,\hat{V}\right)_u\left(\vec{\sigma}\cdot\hat{\vec{r}}_O\right)|\lambda_\nu\rangle \\ &+\frac{1}{c}\sigma_u\langle\lambda_\mu|\hat{V}|\lambda_\nu\rangle \end{aligned} \tag{69}$$

Note that for the position vector $\vec{r}$ the subscript μ is replaced by the common gauge origin O compared to Sec. 2.4. The derivative of the X2C Hamiltonian becomes

$$\boldsymbol{h}_u^{+,B} = \boldsymbol{R}_u^{\dagger,B}\boldsymbol{L}\boldsymbol{R} + \boldsymbol{R}^\dagger\boldsymbol{L}_u^B\boldsymbol{R} + \boldsymbol{R}^\dagger\boldsymbol{L}\boldsymbol{R}_u^B \tag{70}$$

where the derivative of the NESC matrix reads

$$\begin{aligned}\boldsymbol{L}_u^B = \ &\boldsymbol{\Pi}_u^{\dagger,B}\boldsymbol{X} + \boldsymbol{\Pi}^\dagger\boldsymbol{X}_u^B + \boldsymbol{X}_u^{\dagger,B}\boldsymbol{\Pi} + \boldsymbol{X}^\dagger\boldsymbol{\Pi}_u^B \\ &+\boldsymbol{X}_u^{\dagger,B}\left(\frac{1}{4c^2}\boldsymbol{W}-\boldsymbol{T}\right)\boldsymbol{X} + \boldsymbol{X}^\dagger\left(\frac{1}{4c^2}\boldsymbol{W}_u^B-\boldsymbol{T}_u^B\right)\boldsymbol{X} + \boldsymbol{X}^\dagger\left(\frac{1}{4c^2}\boldsymbol{W}-\boldsymbol{T}\right)\boldsymbol{X}_u^B \end{aligned} \tag{71}$$

Compared to the GIAO-based equation, only the derivative of the potential matrix $\boldsymbol{V}$ is omitted.

As the derivative of $\boldsymbol{T}$ is still non-zero, the derivative of the 4c metric $\mathbb{M}$ is also non-zero in RMB. Thus, the working equations for the derivative of $\boldsymbol{X}$ are

$$\boldsymbol{X}_u^B = \left(\boldsymbol{C}_-^S - \boldsymbol{X}\mathbf{C}_-^L\right)\ \left(\boldsymbol{U}_u^B\right)_{-+}\ \boldsymbol{C}_+^{L,\dagger}\ \tilde{\boldsymbol{S}} \tag{72}$$

with the orbital rotation matrix

$$(\boldsymbol{U}_{u,-+}^B)_{kl} = \frac{(\tilde{\boldsymbol{D}}_{u,-+}^B)_{kl} - (\tilde{\boldsymbol{M}}_{u,-+}^B)_{kl}\ (\boldsymbol{E}_{++})_{ll}}{(\boldsymbol{E}_{++})_{ll} - (\boldsymbol{E}_{--})_{kk}} \tag{73}$$

The derivatives of the Dirac matrix and the metric of the Dirac equation are transformed to the basis of the unperturbed solutions according to

$$\begin{aligned}
\tilde{\boldsymbol{D}}_{u,-+}^B &= \boldsymbol{C}_-^{L,\dagger}\boldsymbol{\Pi}_u^{\dagger,B}\boldsymbol{C}_+^S + \boldsymbol{C}_-^{S,\dagger}\boldsymbol{\Pi}_u^B\boldsymbol{C}_+^L \\
&\quad + \frac{1}{4c^2}\boldsymbol{C}_-^{S,\dagger}\boldsymbol{W}_u^B\boldsymbol{C}_+^S - \boldsymbol{C}_-^{S,\dagger}\boldsymbol{T}_u^B\boldsymbol{C}_+^S \tag{74} \\
\tilde{\boldsymbol{M}}_{u,-+}^B &= \frac{1}{2c^2}\boldsymbol{C}_-^{S,\dagger}\boldsymbol{T}_u^B\boldsymbol{C}_+^S \tag{75}
\end{aligned}$$

Furthermore, the derivatives of the renormalization matrix are calculated by solving a simplified version of the Sylvester matrix equation according to

$$\boldsymbol{R}\boldsymbol{R}_u^B + \boldsymbol{R}_u^B\boldsymbol{R} = -\tilde{\boldsymbol{S}}^{-1}\tilde{\boldsymbol{S}}_u^B\boldsymbol{R}\boldsymbol{R} \tag{76}$$

using a generalized eigenvalue decomposition method.[56] The derivative of $\tilde{\boldsymbol{S}}$ is given by

$$\tilde{\boldsymbol{S}}_u^B = \frac{1}{2c^2}\boldsymbol{X}_u^{\dagger,B}\boldsymbol{T}\boldsymbol{X} + \frac{1}{2c^2}\boldsymbol{X}^\dagger\boldsymbol{T}_u^B\boldsymbol{X} + \frac{1}{2c^2}\boldsymbol{X}^\dagger\boldsymbol{T}\boldsymbol{X}_u^B \tag{77}$$

40

A.2 Simplification with Kinetic Balance

Further approximations are possible, i.e. the generalized momentum operator can be neglected like in 4c approaches.[28,29] Thus, the basis set expansion reads[78]

$$\left|\psi_i^L\right\rangle \;=\; \sum_\mu c_{\mu i}^L |\phi_\mu\rangle \tag{78}$$

$$\left|\psi_i^S\right\rangle \;=\; \sum_\mu c_{\mu i}^S \frac{1}{2c}\vec{\sigma}\cdot\hat{\vec{p}}|\phi_\mu\rangle \tag{79}$$

The Dirac equation in the supermatrix form consists of the block-diagonal matrices

$$\boldsymbol{S} \;=\; \begin{pmatrix} \mathbf{S} & 0 \\ 0 & \mathbf{S} \end{pmatrix}, \mathbf{S}_{\mu\nu} = \langle\lambda_\mu|\lambda_\nu\rangle \tag{80}$$

$$\boldsymbol{V} \;=\; \begin{pmatrix} \mathbf{V} & 0 \\ 0 & \mathbf{V} \end{pmatrix}, \mathbf{V}_{\mu\nu} = \langle\lambda_\mu|\hat{V}|\lambda_\nu\rangle \tag{81}$$

$$\boldsymbol{T} \;=\; \begin{pmatrix} \mathbf{T} & 0 \\ 0 & \mathbf{T} \end{pmatrix}, \mathbf{T}_{\mu\nu} = \frac{1}{2}\langle\phi_\mu|\hat{p}^2|\phi_\nu\rangle \tag{82}$$

and the general matrices

$$\boldsymbol{\Pi}_{\mu\nu}^\dagger \;=\; \frac{1}{2}\langle\phi_\mu|\left[\vec{\sigma}\cdot(\hat{\vec{p}}+\frac{1}{c}\hat{\vec{\mathcal{A}}}_O)\right]\left(\vec{\sigma}\cdot\hat{\vec{p}}\right)|\phi_\nu\rangle \tag{83}$$

$$\boldsymbol{W}_{\mu\nu} \;=\; \langle\phi_\mu|\left(\vec{\sigma}\cdot\hat{\vec{p}}\right)\hat{V}\left(\vec{\sigma}\cdot\hat{\vec{p}}\right)|\phi_\nu\rangle \tag{84}$$

Only the generalized momentum matrix $\boldsymbol{\Pi}$ depends on the vector potential. Therefore, the derivative of the X2C Hamiltonian is considerably simplified to

$$h_u^{+,B} = \boldsymbol{R}_u^{\dagger,B}\boldsymbol{L}\boldsymbol{R} + \boldsymbol{R}^\dagger\boldsymbol{L}_u^B\boldsymbol{R} + \boldsymbol{R}^\dagger\boldsymbol{L}\boldsymbol{R}_u^B \tag{85}$$

41

where the derivative of the NESC matrix reads

$$
\begin{aligned}
\boldsymbol{L}_u^B = \quad & \boldsymbol{\Pi}_u^{\dagger,B}\boldsymbol{X} + \boldsymbol{\Pi}^\dagger\boldsymbol{X}_u^B + \boldsymbol{X}_u^{\dagger,B}\boldsymbol{\Pi} + \boldsymbol{X}^\dagger\boldsymbol{\Pi}_u^B \\
& + \boldsymbol{X}_u^{\dagger,B}\left(\frac{1}{4c^2}\boldsymbol{W} - \boldsymbol{T}\right)\boldsymbol{X} + \boldsymbol{X}^\dagger\left(\frac{1}{4c^2}\boldsymbol{W} - \boldsymbol{T}\right)\boldsymbol{X}_u^B
\end{aligned}
\tag{86}
$$

Here, the one-electron integral derivative of the generalized momentum matrix is given by

$$
\begin{aligned}
\left(\frac{\partial\boldsymbol{\Pi}_{\mu\nu}^\dagger}{\partial B_u}\right)_0 &= \frac{1}{4c}\langle\phi_\mu|\left(\hat{\vec{r}}_O\times\vec{\sigma}\right)_u\vec{\sigma}\cdot\hat{\vec{p}}|\phi_\nu\rangle \\
&= \frac{1}{4c}\sigma_0\langle\lambda_\mu|(\hat{\vec{r}}_O\times\hat{\vec{p}})_u|\lambda_\nu\rangle + \frac{\mathrm{i}}{4c}\langle\lambda_\mu|\left[\vec{\sigma}\cdot\hat{\vec{r}}_O\right]\hat{p}_u - \sigma_u\left[\hat{\vec{r}}_O\cdot\hat{\vec{p}}\right]|\lambda_\nu\rangle
\end{aligned}
\tag{87}
$$

Thus, only the prefactor of the scalar part is changed compared to the RMB integral of this derivative. The explicit working equations for the decoupling derivatives read

$$
\boldsymbol{X}_u^B = \left(\boldsymbol{C}_-^S - \boldsymbol{X}\boldsymbol{C}_-^L\right)\ \left(\boldsymbol{U}_u^B\right)_{-+}\ \boldsymbol{C}_+^{L,\dagger}\ \tilde{\boldsymbol{S}}
\tag{88}
$$

with the orbital rotation matrix

$$
(\boldsymbol{U}_{u,-+}^B)_{kl} = \frac{(\tilde{\boldsymbol{D}}_{u,-+}^B)_{kl}}{(\boldsymbol{E}_{++})_{ll} - (\boldsymbol{E}_{--})_{kk}}
\tag{89}
$$

as the derivatives of the metric vanish. The derivatives of the Dirac matrix are transformed to the basis of the unperturbed solutions according to

$$
\tilde{\boldsymbol{D}}_{u,-+}^B = \boldsymbol{C}_-^{L,\dagger}\boldsymbol{\Pi}_u^{\dagger,B}\boldsymbol{C}_+^S + \boldsymbol{C}_-^{S,\dagger}\boldsymbol{\Pi}_u^B\boldsymbol{C}_+^L
\tag{90}
$$

Furthermore, the derivatives of the renormalization matrix are calculated by solving a simplified version of the Sylvester matrix equation according to

$$
\boldsymbol{R}\boldsymbol{R}_u^B + \boldsymbol{R}_u^B\boldsymbol{R} = -\tilde{\boldsymbol{S}}^{-1}\tilde{\boldsymbol{S}}_u^B\boldsymbol{R}\boldsymbol{R}
\tag{91}
$$

using a generalized eigenvalue decomposition method.[56] The derivative of $\tilde{\boldsymbol{S}}$ is given by

$$\tilde{\boldsymbol{S}}_u^B = \frac{1}{2c^2} \boldsymbol{X}_u^{\dagger,B} \boldsymbol{T} \boldsymbol{X} + \frac{1}{2c^2} \boldsymbol{X}^\dagger \boldsymbol{T} \boldsymbol{X}_u^B \tag{92}$$

Thus, the response and Sylvester matrix equations feature the same structural form as for the hyperfine coupling tensor.[73]

A.3 Pseudo-Contact Shift for paramagnetic NMR

The evaluation of the EPR hyperfine coupling matrix and the g-matrix further extends to the hyperfine contribution to the paramagnetic NMR (pNMR) shielding tensor $\boldsymbol{\sigma}_I$ of nucleus I according to[236]

$$\boldsymbol{\sigma}_I^{\text{tot}} = \boldsymbol{\sigma}_I^{\text{orb}} - \frac{\mu_e \tilde{S}(\tilde{S}+1)}{3\gamma_I k_B T} \boldsymbol{A}_I \boldsymbol{g}^{\text{T}} \tag{93}$$

where μ_e denotes the Bohr magneton, γ_I the gyromagnetic ratio, k_B the Boltzmann constant, and T the temperature. $\tilde{S}$ is the expectation value of the effective spin. Note that we use the canonical form of the shielding tensor.[237,238] Here, we neglected zero-field splitting. Composing the HFC and the g-tensor into its isotropic and anisotropic contribution is done via

$$\boldsymbol{M} = M^{\text{iso}} + \boldsymbol{M}^{\text{aniso}} \tag{94}$$

$$M^{\text{iso}} = \frac{1}{3} \operatorname{tr}(\boldsymbol{M}) \tag{95}$$

$$\boldsymbol{M}^{\text{aniso}} = \boldsymbol{M} - M^{\text{iso}} \mathbf{1} \tag{96}$$

Note that this partitioning is necessary due to spin–orbit coupling as discussed in Ref. 236. Therefore, the two-component form of the Fermi-contact (FC) and the pseudo-contact (PC) contribution to the pNMR shielding constant reads

$$\sigma_I^{\text{FC}} = \frac{\mu_e \tilde{S}(\tilde{S}+1)}{3\gamma_I k_B T} A^{\text{iso}} g^{\text{iso}} \tag{97}$$

$$\sigma_I^{\mathrm{PC}} \;\; = \;\; \frac{\mu_e \tilde{S}(\tilde{S}+1)}{3\gamma_I k_B T} \operatorname{tr}\left(\boldsymbol{A}^{\mathrm{aniso}} \boldsymbol{g}^{\mathrm{aniso,\, T}}\right) \tag{98}$$

The FC and the PC term for pNMR can be readily evaluated with the presented X2C implementation as demonstrated in the Supporting Information.

Acknowledgement

Supporting Information Available

Supporting Information is available

- Further studies on the relativistic Hamiltonian, the basis set, density functional approximation, and the impact of the structure for the set of diatomic molecules in Sec. 5 (PDF)

- Comparison of the SNSO and mSNSO approximation to the one-electron X2C ansatz without corrections for Sec. 6.1 (PDF)

- Results and assessment of DLU error for the Sapporo basis sets featuring diffuse functions for Sec. 6.1 (PDF)

- Individual results for the basis set study in Sec. 6.2 (PDF)

- Individual results for the DFT study in Sec. 6.3 (PDF)

- Results for the lanthanide compounds of Sec. 7 with the x2c-QZVPall-2c basis set (PDF)

- Application of the g-tensor and HFC implementation to calculate the temperature-dependent terms for pNMR shielding constants as outlined in Sec. A.3 (PDF)

- Uncontracted x2c-type basis sets for Sec. 6.2, i.e. x2c-SVPall-2c-s and x2c-TZVPall-2c-s (txt)

References

(1) Kaupp, M., Bühl, M., Malkin, V. G., Eds. *Calculation of NMR and EPR Parameters: Theory and Applications*; Wiley-VCH: Weinheim, Germany, 2004.

(2) Neese, F. Quantum Chemistry and EPR Parameters. In *eMagRes*; American Cancer Society, 2017; Vol. 6; pp 1–22.

(3) McWeeny, R. On the Origin of Spin–Hamiltonian Parameters. *J. Phys. Chem.* **1965**, *42*, 1717–1725.

(4) McWeeny, R. *Spins in Quantum Chemistry*; Academic Press: New York, USA, 1970.

(5) Harriman, J. E. *Theoretical Foundations of Electron Spin Resonance*; Physical Chemistry: A Series of Monographs; Academic Press: New York, USA, 1978; Vol. 37.

(6) McWeeny, R. *Methods of molecular quantum mechanics*, 2nd ed.; Academic Press: London, United Kingdom, 1989.

(7) Goldfarb, D., Stoll, S., Eds. *EPR Spectroscopy: Fundamentals and Methods*; John Wiley & Sons: Chichester, United Kingdom, 2018.

(8) Kundu, K.; White, J. R. K.; Moehring, S. A.; Yu, J. M.; Ziller, J. W.; Furche, F.; Evans, W. J.; Hill, S. Clock Transition Due to a Record 1240 G Hyperfine Interaction in a Lu(II) Molecular Spin Qubit. *ChemRxiv* **2021**, DOI: 10.26434/chemrxiv.14399333.v1.

(9) Briganti, M.; Lucaccini, E.; Chelazzi, L.; Ciattini, S.; Sorace, L.; Sessoli, R.; Totti, F.; Perfetti, M. Magnetic Ansiotropy Trends along a Full 4f-Series: The f^{n+7} Effect. *J. Am. Chem. Soc.* **2021**, *143*, 8108–815.

(10) Pyykkö, P. Relativistic Effects in Chemistry: More Common Than You Thought. *Annu. Rev. Phys. Chem.* **2012**, *63*, 45–64.

(11) Saue, T. Relativistic Hamiltonians for Chemistry: A Primer. *ChemPhysChem* **2011**, *12*, 3077–3094.

(12) Dyall, K. G.; Fægri Jr., K. *Introduction to Relativistic Quantum Chemistry*; Oxford University Press: New York, USA, 2007.

(13) Reiher, M.; Wolf., A. *Relativistic Quantum Chemistry – The Fundamental Theory of Molecular Science*, 2nd ed.; Wiley-VCH: Weinheim, Germany, 2015.

(14) Liu, W. Ideas of relativistic quantum chemistry. *Mol. Phys.* **2010**, *108*, 1679–1706.

(15) Liu, W., Ed. *Handbook of Relativistic Quantum Chemistry*; Springer: Berlin, Heidelberg, Germany, 2017.

(16) Liu, W. Essentials of relativistic quantum chemistry. *J. Chem. Phys.* **2020**, *152*, 180901.

(17) Autschbach, J. Relativistic Effects on Magnetic Resonance Parameters and Other Properties of Inorganic Molecules and Metal Complexes. In *Relativistic Methods for Chemists*; Barysz, M., Ishikawa, Y., Eds.; Springer Netherlands: Dordrecht, The Netherlands, 2010; pp 521–598.

(18) Autschbach, J. Perspective: Relativistic effects. *J. Chem. Phys.* **2012**, *136*, 150902.

(19) Autschbach, J. Relativistic calculations of magnetic resonance parameters: background and some recent developments. *Phil. Trans. R. Soc. A.* **2014**, *372*, 20120489.

(20) Chang, C.; Pelissier, M.; Durand, P. Regular Two-Component Pauli-Like Effective Hamiltonians in Dirac Theory. *Phys. Scr.* **1986**, *34*, 394–404.

(21) van Lenthe, E.; Baerends, E. J.; Snijders, J. G. Relativistic regular two-component Hamiltonians. *J. Phys. Chem.* **1993**, *99*, 4597–4610.

(22) van Lenthe, E.; Baerends, E. J.; Snijders, J. G. Relativistic total energy using regular approximations. *J. Chem. Phys.* **1994**, *101*, 9783–9792.

(23) van Lenthe, E.; Wormer, P. E. S.; van der Avoird, A. Density functional calculations of molecular g-tensors in the zero-order regular approximation for relativistic effects. *J. Chem. Phys.* **1997**, *107*, 2488–2498.

(24) Autschbach, J.; Pritchard, B. Calculation of molecular g-tensors using the zeroth-order regular approximation and density functional theory: expectation value versus linear response approaches. *Theor. Chem. Acc.* **2011**, *129*, 453–466.

(25) Aquino, F.; Govind, N.; Autschbach, J. Scalar Relativistic Computations of Nuclear Magnetic Shielding and g-Shifts with the Zeroth-Order Regular Approximation and Range-Separated Hybrid Density Functionals. *J. Chem. Theory Comput.* **2011**, *7*, 3278–3292.

(26) Verma, P.; Autschbach, J. Variational versus Perturbational Treatment of Spin–Orbit Coupling in Relativistic Density Functional Calculations of Electronic g Factors: Effects from Spin-Polarization and Exact Exchange. *J. Chem. Theory Comput.* **2013**, *9*, 1052–1067.

(27) Malkin, I.; Malkina, O. L.; Malkin, V. G.; Kaupp, M. Relativistic two-component calculations of electronic g-tensors that include spin polarization. *J. Chem. Phys.* **2005**, *123*, 244103.

(28) Repiský, M.; Komorovský, S.; Malkin, E.; Malkina, O. L.; Malkin, V. G. Relativistic four-component calculations of electronic g-tensors in the matrix Dirac–Kohn–Sham framework. *Chem. Phys. Lett.* **2010**, *488*, 94–97.

(29) Gohr, S.; Hrobárik, P.; Repiský, M.; Komorovský, S.; Ruud, K.; Kaupp, M. Four-Component Relativistic Density Functional Theory Calculations of EPR g- and Hyperfine-Coupling Tensors Using Hybrid Functionals: Validation on Transition-Metal Complexes with Large Tensor Anisotropies and Higher-Order Spin–Orbit Effects. *J. Phys. Chem. A* **2015**, *119*, 12892–12905.

(30) Cherry, P. J.; Komorovsky, S.; Malkin, V. G.; Malkina, O. L. Calculations of the EPR g-tensor using unrestricted two- and four-component relativistic approaches within the HF and DFT frameworks. *Mol. Phys.* **2017**, *115*, 75–89.

(31) Remigio, R. D.; Repisky, M.; Komorovsky, S.; Hrobarik, P.; Frediani, L.; Ruud, K. Four-component relativistic density functional theory with the polarisable continuum model: application to EPR parameters and paramagnetic NMR shifts. *Mol. Phys.* **2017**, *115*, 214–227.

(32) Kutzelnigg, W.; Liu, W. Quasirelativistic theory equivalent to fully relativistic theory. *J. Chem. Phys.* **2005**, *123*, 241102.

(33) Liu, W.; Kutzelnigg, W. Quasirelativistic theory. II. Theory at matrix level. *J. Chem. Phys.* **2007**, *126*, 114107.

(34) Liu, W.; Peng, D. Infinite-order quasirelativistic density functional method based on the exact matrix quasirelativistic theory. *J. Chem. Phys.* **2006**, *125*, 044102.

(35) Liu, W.; Peng, D. Erratum: "Infinite-order quasirelativistic density functional method based on the exact matrix quasirelativistic theory" [J. Chem. Phys. 125, 044102 (2006)]. *J. Chem. Phys.* **2006**, *125*, 149901.

(36) Iliaš, M.; Saue, T. An infinite-order two-component relativistic Hamiltonian by a simple one-step transformation. *J. Chem. Phys.* **2007**, *126*, 064102.

(37) Liu, W.; Peng, D. Exact two-component Hamiltonians revisited. *J. Chem. Phys.* **2009**, *131*, 031104.

(38) Peng, D.; Liu, W.; Xiao, Y.; Cheng, L. Making four- and two-component relativistic density functional methods fully equivalent based on the idea of "from atoms to molecule". *J. Chem. Phys.* **2007**, *127*, 104106.

(39) Repisky, M.; Komorovsky, S.; Kadek, M.; Konecny, L.; Ekström, U.; Malkin, E.; Kaupp, M.; Ruud, K.; Malkina, O. L.; Malkin, V. G. ReSpect: Relativistic spectroscopy DFT program package. *J. Chem. Phys.* **2020**, *152*, 184101.

(40) Zhang, Y.; Suo, B.; Wang, Z.; Zhang, N.; Li, Z.; Lei, Y.; Zou, W.; Gao, J.; Peng, D.; Pu, Z.; Xiao, Y.; Sun, Q.; Wang, F.; Ma, Y.; Wang, X.; Guo, Y.; Liu, W. BDF: A relativistic electronic structure program package. *J. Chem. Phys.* **2020**, *152*, 064113.

(41) Saue, T.; Bast, R.; Gomes, A. S. P.; Jensen, H. J. A.; Visscher, L.; Aucar, I. A.; Di Remigio, R.; Dyall, K. G.; Eliav, E.; Fasshauer, E.; Fleig, T.; Halbert, L.; Hedegård, E. D.; Helmich-Paris, B.; Iliaš, M.; Jacob, C. R.; Knecht, S.; Laerdahl, J. K.; Vidal, M. L.; Nayak, M. K.; Olejniczak, M.; Olsen, J. M. H.; Pernpointner, M.; Senjean, B.; Shee, A.; Sunaga, A.; van Stralen, J. N. P. The DIRAC code for relativistic molecular calculations. *J. Chem. Phys.* **2020**, *152*, 204104.

(42) Williams-Young, D. B.; Petrone, A.; Sun, S.; Stetina, T. F.; Lestrange, P.; Hoyer, C. E.; Nascimento, D. R.; Koulias, L.; Wildman, A.; Kasper, J.; Goings, J. J.; Ding, F.;

DePrince III, A. E.; Valeev, E. F.; Li, X. The Chronus Quantum software package. *Wiley Interdiscip. Rev.: Comput. Mol. Sci.* **2020**, *10*, e1436.

(43) Werner, H.-J.; Knowles, P. J.; Manby, F. R.; Black, J. A.; Doll, K.; Heßel-mann, A.; Kats, D.; Köhn, A.; Korona, T.; Kreplin, D. A.; Ma, Q.; Miller, T. F.; Mitrushchenkov, A.; Peterson, K. A.; Polyak, I.; Rauhut, G.; Sibaev, M. The Molpro quantum chemistry package. *J. Chem. Phys.* **2020**, *152*, 144107.

(44) Aquilante, F.; Autschbach, J.; Carlson, R. K.; Chibotaru, L. F.; Delcey, M. G.; De Vico, L.; Fdez. Galván, I.; Ferré, N.; Frutos, L. M.; Gagliardi, L.; Garavelli, M.; Giussani, A.; Hoyer, C. E.; Li Manni, G.; Lischka, H.; Ma, D.; Malmqvist, P. Å.; Müller, T.; Nenov, A.; Olivucci, M.; Pedersen, T. B.; Peng, D.; Plasser, F.; Pritchard, B.; Reiher, M.; Rivalta, I.; Schapiro, I.; Segarra-Martí, J.; Stenrup, M.; Truhlar, D. G.; Ungur, L.; Valentini, A.; Vancoillie, S.; Veryazov, V.; Vysotskiy, V. P.; Weingart, O.; Zapata, F.; Lindh, R. Molcas 8: New capabilities for multiconfigura-tional quantum chemical calculations across the periodic table. *J. Comput. Chem.* **2016**, *37*, 506–.541.

(45) Matthews, D. A.; Cheng, L.; Harding, M. E.; Lipparini, F.; Stopkowicz, S.; Jagau, T.-C.; Szalay, P. G.; Gauss, J.; Stanton, J. F. Coupled-cluster techniques for computa-tional chemistry: The CFOUR program package. *J. Chem. Phys.* **2020**, *152*, 214108.

(46) Smith, D. G. A.; Burns, L. A.; Simmonett, A. C.; Parrish, R. M.; Schieber, M. C.; Galvelis, R.; Kraus, P.; Kruse, H.; Di Remigio, R.; Alenaizan, A.; James, A. M.; Lehtola, S.; Misiewicz, J. P.; Scheurer, M.; Shaw, R. A.; Schriber, J. B.; Xie, Y.; Glick, Z. L.; Sirianni, D. A.; O'Brien, J. S.; Waldrop, J. M.; Kumar, A.; Ho-henstein, E. G.; Pritchard, B. P.; Brooks, B. R.; Schaefer, H. F.; Sokolov, A. Y.; Patkowski, K.; DePrince, A. E.; Bozkaya, U.; King, R. A.; Evangelista, F. A.; Tur-ney, J. M.; Crawford, T. D.; Sherrill, C. D. PSI4 1.4: Open-source software for high-throughput quantum chemistry. *J. Phys. Chem.* **2020**, *152*, 184108.

(47) Aprà, E.; Bylaska, E. J.; de Jong, W. A.; Govind, N.; Kowalski, K.; Straatsma, T. P.; Valiev, M.; van Dam, H. J. J.; Alexeev, Y.; Anchell, J.; Anisimov, V.; Aquino, F. W.; Atta-Fynn, R.; Autschbach, J.; Bauman, N. P.; Becca, J. C.; Bernholdt, D. E.; Bhaskaran-Nair, K.; Bogatko, S.; Borowski, P.; Boschen, J.; Brabec, J.; Bruner, A.; Cauët, E.; Chen, Y.; Chuev, G. N.; Cramer, C. J.; Daily, J.; Deegan, M. J. O.; Dunning, T. H.; Dupuis, M.; Dyall, K. G.; Fann, G. I.; Fischer, S. A.; Fonari, A.; Früchtl, H.; Gagliardi, L.; Garza, J.; Gawande, N.; Ghosh, S.; Glaesemann, K.; Götz, A. W.; Hammond, J.; Helms, V.; Hermes, E. D.; Hirao, K.; Hirata, S.; Jacquelin, M.; Jensen, L.; Johnson, B. G.; Jónsson, H.; Kendall, R. A.; Klemm, M.; Kobayashi, R.; Konkov, V.; Krishnamoorthy, S.; Krishnan, M.; Lin, Z.; Lins, R. D.; Littlefield, R. J.; Logsdail, A. J.; Lopata, K.; Ma, W.; Marenich, A. V.; Martin del Campo, J.; Mejia-Rodriguez, D.; Moore, J. E.; Mullin, J. M.; Nakajima, T.; Nascimento, D. R.; Nichols, J. A.; Nichols, P. J.; Nieplocha, J.; Otero-de-la Roza, A.; Palmer, B.; Panyala, A.; Pirojsirikul, T.; Peng, B.; Peverati, R.; Pittner, J.; Pollack, L.; Richard, R. M.; Sadayappan, P.; Schatz, G. C.; Shelton, W. A.; Silverstein, D. W.; Smith, D. M. A.; Soares, T. A.; Song, D.; Swart, M.; Taylor, H. L.; Thomas, G. S.; Tipparaju, V.; Truhlar, D. G.; Tsemekhman, K.; Van Voorhis, T.; Vázquez-Mayagoitia, A.; Verma, P.; Villa, O.; Vishnu, A.; Vogiatzis, K. D.; Wang, D.; Weare, J. H.; Williamson, M. J.; Windus, T. L.; Woliński, K.; Wong, A. T.; Wu, Q.; Yang, C.; Yu, Q.; Zacharias, M.; Zhang, Z.; Zhao, Y.; Harrison, R. J. NWChem: Past, present, and future. *J. Chem. Phys.* **2020**, *152*, 184102.

(48) Balasubramani, S. G.; Chen, G. P.; Coriani, S.; Diedenhofen, M.; Frank, M. S.; Franzke, Y. J.; Furche, F.; Grotjahn, R.; Harding, M. E.; Hättig, C.; Hellweg, A.; Helmich-Paris, B.; Holzer, C.; Huniar, U.; Kaupp, M.; Marefat Khah, A.; Karbalaei Khani, S.; Müller, T.; Mack, F.; Nguyen, B. D.; Parker, S. M.; Perlt, E.; Rappoport, D.; Reiter, K.; Roy, S.; Rückert, M.; Schmitz, G.; Sierka, M.; Tapavicza, E.; Tew, D. P.; van Wüllen, C.; Voora, V. K.; Weigend, F.; Wodyński, A.; Yu, J. M. TUR-

BOMOLE: Modular program suite for *ab initio* quantum-chemical and condensed-matter simulations. *J. Chem. Phys.* **2020**, *152*, 184107.

(49) Cheng, L.; Stopkowicz, S.; Gauss, J. Analytic energy derivatives in relativistic quantum chemistry. *Int. J. Quantum Chem.* **2014**, *114*, 1108–1127.

(50) Cremer, D.; Zou, W.; Filatov, M. Dirac-exact relativistic methods: the normalized elimination of the small component method. *Wiley Interdiscip. Rev.: Comput. Mol. Sci.* **2014**, *4*, 436–467.

(51) Nakajima, T.; Hirao, K. The Douglas–Kroll–Hess Approach. *Chem. Rev.* **2012**, *112*, 385–402.

(52) Reiher, M. Relativistic Douglas–Kroll–Hess theory. *Wiley Interdiscip. Rev.: Comput. Mol. Sci.* **2012**, *2*, 139–149.

(53) Zou, W.; Filatov, M.; Cremer, D. Development and application of the analytical energy gradient for the normalized elimination of the small component method. *J. Chem. Phys.* **2011**, *134*, 244117.

(54) Cheng, L.; Gauss, J. Analytic energy gradients for the spin-free exact two-component theory using an exact block diagonalization for the one-electron Dirac Hamiltonian. *J. Chem. Phys.* **2011**, *135*, 084114.

(55) Cheng, L.; Gauss, J. Analytic second derivatives for the spin-free exact two-component theory. *J. Chem. Phys.* **2011**, *135*, 244104.

(56) Zou, W.; Filatov, M.; Cremer, D. Development, Implementation, and Application of an Analytic Second Derivative Formalism for the Normalized Elimination of the Small Component Method. *J. Chem. Theory Comput.* **2012**, *8*, 2617–2629.

(57) Zou, W.; Filatov, M.; Cremer, D. Analytical energy gradient for the two-component

normalized elimination of the small component method. *J. Chem. Phys.* **2015**, *142*, 214106.

(58) Franzke, Y. J.; Middendorf, N.; Weigend, F. Efficient implementation of one- and two-component analytical energy gradients in exact two-component theory. *J. Chem. Phys.* **2018**, *148*, 104110.

(59) Zou, W.; Guo, G.; Suo, B.; Liu, W. Analytic Energy Gradients and Hessians of Exact Two-Component Relativistic Methods: Efficient Implementation and Extensive Applications. *J. Chem. Theory Comput.* **2020**, *16*, 1541–1554.

(60) Filatov, M.; Zou, W.; Cremer, D. Analytic Calculation of Contact Densities and Mössbauer Isomer Shifts Using the Normalized Elimination of the Small-Component Formalism. *J. Chem. Theory Comput.* **2012**, *8*, 875–882.

(61) Yoshizawa, T.; Zou, W.; Cremer, D. Calculations of electric dipole moments and static dipole polarizabilities based on the two-component normalized elimination of the small component method. *J. Chem. Phys.* **2016**, *145*, 184104.

(62) Yoshizawa, T.; Filatov, M.; Cremer, D.; Zou, W. Calculation of contact densities and Mössbauer isomer shifts utilising the Dirac-exact two-component normalised elimination of the small component (2c-NESC) method. *Mol. Phys.* **2019**, *117*, 1164–1171.

(63) Zhu, H.; Gao, C.; Filatov, M.; Zou, W. Mössbauer isomer shifts and effective contact densities obtained by the exact two-component (X2C) relativistic method and its local variants. *Phys. Chem. Chem. Phys.* **2020**, *22*, 26776–26786.

(64) Sun, Q.; Liu, W.; Xiao, Y.; Cheng, L. Exact two-component relativistic theory for nuclear magnetic resonance parameters. *J. Chem. Phys.* **2009**, *131*, 081101.

(65) Sun, Q.; Xiao, Y.; Liu, W. Exact two-component relativistic theory for NMR parameters: General formulation and pilot application. *J. Chem. Phys.* **2012**, *137*, 174105.

(66) Cheng, L.; Gauss, J.; Stanton, J. F. Treatment of scalar-relativistic effects on nuclear magnetic shieldings using a spin-free exact-two-component approach. *J. Chem. Phys.* **2013**, *139*, 054105.

(67) Yoshizawa, T.; Zou, W.; Cremer, D. Calculations of atomic magnetic nuclear shielding constants based on the two-component normalized elimination of the small component method. *J. Chem. Phys.* **2017**, *146*, 134109.

(68) Yoshizawa, T.; Hada, M. Calculations of nuclear magnetic shielding constants based on the exact two-component relativistic method. *J. Chem. Phys.* **2017**, *147*, 154104.

(69) Yoshizawa, T. On the development of the exact two-component relativistic method for calculating indirect NMR spin-spin coupling constants. *Chem. Phys.* **2019**, *518*, 112–122.

(70) Franzke, Y. J.; Weigend, F. NMR Shielding Tensors and Chemical Shifts in Scalar-Relativistic Local Exact Two-Component Theory. *J. Chem. Theory Comput.* **2019**, *15*, 1028–1043.

(71) Franzke, Y. J.; Mack, F.; Weigend, F. NMR Indirect Spin–Spin Coupling Constants in a Modern Quasirelativistic Density Functional Framework. *J. Chem. Theory Comput.* **2021**, *17*, 3974–3994.

(72) Filatov, M.; Zou, W.; Cremer, D. Analytic Calculation of Isotropic Hyperfine Structure Constants Using the Normalized Elimination of the Small Component Formalism. *J. Phys. Chem. A* **2012**, *116*, 3481–3486.

(73) Franzke, Y. J.; Yu, J. M. Hyperfine Coupling Constants in Local Exact Two-Component Theory. *ChemRxiv* **2021**, DOI: 10.33774/chemrxiv-2021-wnz1v-v2.

(74) Gillhuber, S.; Franzke, Y. J.; Weigend, F. Paramagnetic NMR Shielding Tensors and

Ring Currents: Efficient Implementation and Application to Heavy Element Compounds. *J. Phys. Chem. A* **2021**, *125*, 9707–9723.

(75) Autschbach, J. Relativistic Effects on Electron–Nucleus Hyperfine Coupling Studied with an Exact 2-Component (X2C) Hamiltonian. *J. Chem. Theory Comput.* **2017**, *13*, 710–718.

(76) Feng, R.; Duignan, T. J.; Autschbach, J. Electron–Nucleus Hyperfine Coupling Calculated from Restricted Active Space Wavefunctions and an Exact Two-Component Hamiltonian. *J. Chem. Theory Comput.* **2021**, *17*, 255–268.

(77) Wodyński, A.; Kaupp, M. Density Functional Calculations of EPR g- and Hyperfine-Coupling Tensors Using the Exact Two-Component (X2C) Transformation and Efficient Approximations to the Two-Electron Spin-Orbit Terms. *J. Phys. Chem. A* **2019**, *123*, 5660–5672.

(78) Stanton, R. E.; Havriliak, S. Kinetic balance: A partial solution to the problem of variational safety in Dirac calculations. *J. Chem. Phys.* **1984**, *81*, 1910–1918.

(79) Komorovský, S.; Repiský, M.; Malkina, O. L.; Malkin, V. G.; Malkin Ondík, I.; Kaupp, M. A fully relativistic method for calculation of nuclear magnetic shielding tensors with a restricted magnetically balanced basis in the framework of the matrix Dirac-Kohn-Sham equation. *J. Chem. Phys.* **2008**, *128*, 104101.

(80) Sun, S.; Li, X. Relativistic Effects in Magnetic Circular Dichroism: Restricted Magnetic Balance and Temperature Dependence. *J. Chem. Theory Comput.* **2020**, *16*, 4533–4542.

(81) Kutzelnigg, W. Ab initio calculation of molecular properties. *J. Mol. Struct.: THEOCHEM* **1989**, *202*, 11–61.

(82) London, F. Théorie quantique des courants interatomiques dans les combinaisons aromatiques. *J. Phys. Radium* **1937**, *8*, 397–409.

(83) Ditchfield, R. Self-consistent perturbation theory of diamagnetism. *Mol. Phys.* **1974**, *27*, 789–807.

(84) Komorovský, S.; Repiský, M.; Malkina, O. L.; Malkin, V. G. Fully relativistic calculations of NMR shielding tensors using restricted magnetically balanced basis and gauge including atomic orbitals. *J. Chem. Phys.* **2010**, *132*, 154101.

(85) Olejniczak, M.; Bast, R.; Saue, T.; Pecul, M. A simple scheme for magnetic balance in four-component relativistic Kohn-Sham calculations of nuclear magnetic resonance shielding constants in a Gaussian basis. *J. Chem. Phys.* **2012**, *136*, 014108.

(86) Olejniczak, M.; Bast, R.; Saue, T.; Pecul, M. Erratum: "A simple scheme for magnetic balance in four-component relativistic Kohn–Sham calculations of nuclear magnetic resonance shielding constants in a Gaussian basis" [J. Chem. Phys. 136, 014108 (2012)]. *J. Chem. Phys.* **2012**, *136*, 239902.

(87) Fukuda, R.; Hada, M.; Nakatsuji, H. Quasirelativistic theory for magnetic shielding constants. II. Gauge-including atomic orbitals and applications to molecules. *J. Phys. Chem.* **2003**, *118*, 1027–1035.

(88) Yoshizawa, T.; Hada, M. Gauge-origin dependence of NMR shielding constants in the Douglas–Kroll–Hess method. *Chem. Phys. Lett.* **2015**, *618*, 132–141.

(89) Hayami, M.; Seino, J.; Nakai, H. Gauge-origin independent formalism of two-component relativistic framework based on unitary transformation in nuclear magnetic shielding constant. *J. Chem. Phys.* **2018**, *148*, 114109.

(90) Wolff, S. K.; Ziegler, T.; van Lenthe, E.; Baerends, E. J. Density functional calculations of nuclear magnetic shieldings using the zeroth-order regular approximation (ZORA)

for relativistic effects: ZORA nuclear magnetic resonance. *J. Chem. Phys.* **1999**, *110*, 7689–7698.

(91) Autschbach, J. The role of the exchange-correlation response kernel and scaling corrections in relativistic density functional nuclear magnetic shielding calculations with the zeroth-order regular approximation. *Mol. Phys.* **2013**, *111*, 2544–2554.

(92) Neese, F.; Solomon, E. I. Calculation of Zero-Field Splittings, g-Values, and the Relativistic Nephelauxetic Effect in Transition Metal Complexes. Application to High-Spin Ferric Complexes. *Inorg. Chem.* **1998**, *37*, 6568–6582.

(93) Tran, V. A.; Neese, F. Double-hybrid density functional theory for g-tensor calculations using gauge including atomic orbitals. *J. Chem. Phys.* **2020**, *153*, 054105.

(94) Schreckenbach, G.; Ziegler, T. Calculation of the G-Tensor of Electron Paramagnetic Resonance Spectroscopy Using Gauge-Including Atomic Orbitals and Density Functional Theory. *J. Phys. Chem. A* **1997**, *101*, 3388–3399.

(95) Schreckenbach, G.; Ziegler, T. Density functional calculations of NMR chemical shifts and ESR g-tensors. *Theor. Chem. Acc.* **1998**, *99*, 71–82.

(96) Patchkovskii, S.; Ziegler, T. Prediction of electron paramagnetic resonance g-tensors of transition metal complexes using density functional theory: First applications to some axial d^1 MEX$_4$ systems. *J. Phys. Chem.* **1999**, *111*, 5730–5740.

(97) Patchkovskii, S.; Ziegler, T. Prediction of EPR g Tensors in Simple d^1 Metal Porphyrins with Density Functional Theory. *J. Am. Chem. Soc.* **2000**, *122*, 3506–3516.

(98) Patchkovskii, S.; Strong, R. T.; Pickard, C. J.; Un, S. Gauge invariance of the spin-other-orbit contribution to the g-tensors of electron paramagnetic resonance. *J. Chem. Phys.* **2005**, *122*, 214101.

(99) Peng, D.; Reiher, M. Local relativistic exact decoupling. *J. Chem. Phys.* **2012**, *136*, 244108.

(100) Zhang, T.; Kasper, J. M.; Li, X. Localized relativistic two-component methods for ground and excited state calculations. In *Annual Reports in Computational Chemistry*; Dixon, D. A., Ed.; Elsevier: Amsterdam, The Netherlands, 2020; Vol. 16; Chapter 2, pp 17–37.

(101) Peng, D.; Middendorf, N.; Weigend, F.; Reiher, M. An efficient implementation of two-component relativistic exact-decoupling methods for large molecules. *J. Chem. Phys.* **2013**, *138*, 184105.

(102) Seino, J.; Nakai, H. Local unitary transformation method for large-scale two-component relativistic calculations: Case for a one-electron Dirac Hamiltonian. *J. Chem. Phys.* **2012**, *136*, 244102.

(103) Seino, J.; Nakai, H. Local unitary transformation method for large-scale two-component relativistic calculations. II. Extension to two-electron Coulomb interaction. *J. Chem. Phys.* **2012**, *137*, 144101.

(104) Lichtenberger, N.; Franzke, Y. J.; Massa, W.; Weigend, F.; Dehnen, S. The Identity of "Ternary" A/Tl/Pb or K/Tl/Bi Solid Mixtures and Binary Zintl Anions Isolated From Their Solutions. *Chem. Eur. J.* **2018**, *24*, 12022–12030.

(105) Balmer, M.; Franzke, Y. J.; Weigend, F.; von Hänisch, C. Low valent group 14 phosphinidenide complexes [(SIDippP)$_2$M] exhibit P-M pπ-pπ interaction (M = Ge, Sn, Pb). *Chem. Eur. J.* **2020**, *26*, 192–197.

(106) Eulenstein, A. R.; Franzke, Y. J.; Bügel, P.; Massa, W.; Weigend, F.; Dehnen, S. Stabilizing a metalloid {Zn$_{12}$} unit within a polymetallide environment in [K$_2$Zn$_{20}$Bi$_{16}$]$^{6-}$. *Nat. Commun.* **2020**, *11*, 5122.

(107) Eulenstein, A. R.; Franzke, Y. J.; Lichtenberger, N.; Wilson, R. J.; Deubner, H. L.; Kraus, F.; Weigend, F.; Dehnen, S. Substantial π-aromaticity of the anionic heavy-metal cluster $[\text{Th@Bi}_{12}]^{4-}$. *Nat. Chem.* **2021**, *13*, 149–155.

(108) Van Wüllen, C. Spin densities in two-component relativistic density functional calculations: Noncollinear versus collinear approach. *J. Comput. Chem.* **2002**, *23*, 779–785.

(109) Verma, P.; Autschbach, J. Relativistic Density Functional Calculations of Hyperfine Coupling with Variational versus Perturbational Treatment of Spin–Orbit Coupling. *J. Chem. Theory Comput.* **2013**, *9*, 1932–1948.

(110) Gell-Mann, M. The interpretation of the new particles as displaced charge multiplets. *Nuovo Cim.* **1956**, *4*, 848–866.

(111) Foldy, L. L.; Wouthuysen, S. A. On the Dirac Theory of Spin 1/2 Particles and Its Non-Relativistic Limit. *Phys. Rev.* **1950**, *78*, 29–36.

(112) Heully, J.-L.; Lindgren, I.; Lindroth, E.; Lundqvist, S.; Mårtensson-Pendrill, A.-M. Diagonalisation of the Dirac Hamiltonian as a basis for a relativistic many-body procedure. *J. Phys. B: At. Mol. Phys.* **1986**, *19*, 2799–2815.

(113) Dyall, K. G. Interfacing relativistic and nonrelativistic methods. I. Normalized elimination of the small component in the modified Dirac equation. *J. Chem. Phys.* **1997**, *106*, 9618–9626.

(114) Dyall, K. G. Interfacing relativistic and nonrelativistic methods. II. Investigation of a low-order approximation. *J. Chem. Phys.* **1998**, *109*, 4201–4208.

(115) Dyall, K. G.; Enevoldsen, T. Interfacing relativistic and nonrelativistic methods. III. Atomic 4-spinor expansions and integral approximations. *J. Chem. Phys.* **1999**, *111*, 10000–10007.

(116) Dyall, K. G. Interfacing relativistic and nonrelativistic methods. IV. One- and two-electron scalar approximations. *J. Chem. Phys.* **2001**, *115*, 9136–9143.

(117) Boettger, J. C. Approximate two-electron spin-orbit coupling term for density-functional-theory DFT calculations using the Douglas-Kroll-Hess transformation. *Phys. Rev. B* **2000**, *62*, 7809–7815.

(118) Filatov, M.; Zou, W.; Cremer, D. Spin-orbit coupling calculations with the two-component normalized elimination of the small component method. *J. Chem. Phys.* **2013**, *139*, 014106.

(119) Pulay, P. Ab initio calculation of force constants and equilibrium geometries in poly-atomic molecules. *Mol. Phys.* **1969**, *17*, 197–204.

(120) Rice, J.; Amos, R. On the efficient evaluation of analytic energy gradients. *Chem. Phys. Lett.* **1985**, *122*, 585–590.

(121) Baldes, A.; Weigend, F. Efficient two-component self-consistent field procedures and gradients: implementation in TURBOMOLE and application to Au_{20}^-. *Mol. Phys.* **2013**, *111*, 2617–2624.

(122) Pausch, A.; Klopper, W. Efficient evaluation of three-centre two-electron integrals over London orbitals. *Mol. Phys.* **2020**, *118*, e1736675.

(123) Wolinski, K.; Hinton, J. F.; Pulay, P. Efficient implementation of the gauge-independent atomic orbital method for NMR chemical shift calculations. *J. Am. Chem. Soc.* **1990**, *112*, 8251–8260.

(124) Häser, M.; Ahlrichs, R.; Baron, H. P.; Weis, P.; Horn, H. Direct computation of second-order scf properties of large molecules on workstation computers with an application to large carbon clusters. *Theor. Chim. Acta* **1992**, *83*, 455–470.

(125) Reiter, K.; Mack, F.; Weigend, F. Calculation of Magnetic Shielding Constants with meta-GGA Functionals Employing the Multipole-Accelerated Resolution of the Identity: Implementation and Assessment of Accuracy and Efficiency. *J. Chem.Theory Comput.* **2018**, *14*, 191–197.

(126) Armbruster, M. K.; Weigend, F.; van Wüllen, C.; Klopper, W. Self-consistent treatment of spin-orbit interactions with efficient Hartree-Fock and density functional methods. *Phys. Chem. Chem. Phys.* **2008**, *10*, 1748–1756.

(127) Krykunov, M.; Ziegler, T.; van Lenthe, E. Implementation of a Hybrid DFT Method for Calculating NMR Shieldings Using Slater-Type Orbitals with Spin–Orbital Coupling Included. Applications to ^{187}Os, ^{195}Pt, and ^{13}C in Heavy-Metal Complexes. *J. Phys. Chem. A* **2009**, *113*, 11495–11500.

(128) Franzke, Y. J. Calculation of NMR Parameters in a Modern Relativistic Density Functional Framework: Theory, Implementation, and Application. Dissertation, Karlsruhe Institute of Technology (KIT), Germany, 2021.

(129) van Wüllen, C.; Michauk, C. Accurate and efficient treatment of two-electron contributions in quasirelativistic high-order Douglas-Kroll density-functional calculations. *J. Chem. Phys.* **2005**, *123*, 204113.

(130) Plessow, P.; Weigend, F. Seminumerical calculation of the Hartree–Fock exchange matrix: Application to two-component procedures and efficient evaluation of local hybrid density functionals. *J. Comput. Chem.* **2012**, *33*, 810–816.

(131) Holzer, C. An improved seminumerical Coulomb and exchange algorithm for properties and excited states in modern density functional theory. *J. Chem. Phys.* **2020**, *153*, 184115.

(132) Pollak, P.; Weigend, F. Segmented Contracted Error-Consistent Basis Sets of Double-

and Triple-ζ Valence Quality for One- and Two-Component Relativistic All-Electron Calculations. *J. Chem. Theory Comput.* **2017**, *13*, 3696–3705.

(133) Ahlrichs, R.; Bär, M.; Häser, M.; Horn, H.; Kölmel, C. Electronic structure calculations on workstation computers: The program system turbomole. *Chem. Phys. Lett.* **1989**, *162*, 165–169.

(134) Furche, F.; Ahlrichs, R.; Hättig, C.; Klopper, W.; Sierka, M.; Weigend, F. Turbomole. *Wiley Interdiscip. Rev.: Comput. Mol. Sci.* **2014**, *4*, 91–100.

(135) Developers' version of TURBOMOLE V7.5.1 2021, a development of University of Karlsruhe and Forschungszentrum Karlsruhe GmbH, 1989-2007, TURBOMOLE GmbH, since 2007; available from `https://www.turbomole.org` (retrieved August 23, 2021).

(136) Huniar, U. Berechnung der chemischen Verschiebung der NMR mit Methoden der Dichtefunktionaltheorie (DFT). Diploma Thesis, University of Karlsruhe (TH), Germany, 1999.

(137) Kollwitz, M.; Gauss, J. A direct implementation of the GIAO-MBPT(2) method for calculating NMR chemical shifts. Application to the naphthalenium and anthracenium ions. *Chem. Phys. Lett.* **1996**, *260*, 639–646.

(138) Kollwitz, M.; Häser, M.; Gauss, J. Non-Abelian point group symmetry in direct second-order many-body perturbation theory calculations of NMR chemical shifts. *J. Chem. Phys.* **1998**, *108*, 8295–8301.

(139) Dupuis, M.; Rys, J.; King, H. F. Evaluation of molecular integrals over Gaussian basis functions. *J. Chem. Phys.* **1976**, *65*, 111–116.

(140) Rys, J.; Dupuis, M.; King, H. F. Computation of electron repulsion integrals using the rys quadrature method. *J. Comput. Chem.* **1983**, *4*, 154–157.

(141) Dupuis, M.; Marquez, A. The Rys quadrature revisited: A novel formulation for the efficient computation of electron repulsion integrals over Gaussian functions. *J. Chem. Phys.* **2001**, *114*, 2067–2078.

(142) Gautschi, W. Algorithm 726: ORTHPOL–a Package of Routines for Generating Orthogonal Polynomials and Gauss-Type Quadrature Rules. *ACM Trans. Math. Softw.* **1994**, *20*, 21–62.

(143) Kehry, M.; Franzke, Y. J.; Holzer, C.; Klopper, W. Quasirelativistic two-component core excitations and polarisabilities from a damped-response formulation of the Bethe–Salpeter equation. *Mol. Phys.* **2020**, *118*, e1755064.

(144) Visscher, L.; Dyall, K. G. Dirac-Fock atomic electronic structure calculations using different nuclear charge distributions. *At. Data Nucl. Data Tables* **1997**, *67*, 207–224.

(145) CODATA internationally recommened 2018 values of the fundamental physical constans, `https://physics.nist.gov/cuu/Constants/index.html` (retrieved December 28, 2020).

(146) Klamt, A.; Schüürmann, G. COSMO: a new approach to dielectric screening in solvents with explicit expressions for the screening energy and its gradient. *J. Chem. Soc., Perkin Trans. 2* **1993**, 799–805.

(147) Schäfer, A.; Klamt, A.; Sattel, D.; Lohrenz, J. C. W.; Eckert, F. COSMO Implementation in TURBOMOLE: Extension of an efficient quantum chemical code towards liquid systems. *Phys. Chem. Chem. Phys.* **2000**, *2*, 2187–2193.

(148) Weigend, F. A fully direct RI-HF algorithm: Implementation, optimised auxiliary basis sets, demonstration of accuracy and efficiency. *Phys. Chem. Chem. Phys.* **2002**, *4*, 4285–4291.

(149) Perdew, J. P.; Schmidt, K. Jacob's ladder of density functional approximations for the exchange-correlation energy. *AIP Conf. Proc.* **2001**, *577*, 1–20.

(150) Becke, A. D. Perspective: Fifty years of density-functional theory in chemical physics. *J. Chem. Phys.* **2014**, *140*, 18A301.

(151) Mardirossian, N.; Head-Gordon, M. Thirty years of density functional theory in computational chemistry: an overview and extensive assessment of 200 density functionals. *Mol. Phys.* **2017**, *115*, 2315–2372.

(152) Maximoff, S. N.; Scuseria, G. E. Nuclear magnetic resonance shielding tensors calculated with kinetic energy density-dependent exchange-correlation functionals. *Chem. Phys. Lett.* **2004**, *390*, 408–412.

(153) Marques, M. A. L.; Oliveira, M. J. T.; Burnus, T. Libxc: A library of exchange and correlation functionals for density functional theory. *Comput. Phys. Commun.* **2012**, *183*, 2272–2281.

(154) Lehtola, S.; Steigemann, C.; Oliveira, M. J. T.; Marques, M. A. L. Recent developments in libxc – A comprehensive library of functionals for density functional theory. *SoftwareX* **2018**, *7*, 1–5.

(155) Libxc. 5.1.4, available from `https://www.tddft.org/programs/libxc/` (retrieved July 30, 2021).

(156) Ekström, U.; Visscher, L.; Bast, R.; Thorvaldsen, A. J.; Ruud, K. Arbitrary-Order Density Functional Response Theory from Automatic Differentiation. *J. Chem. Theory Comput.* **2010**, *6*, 1971–1980.

(157) Reiter, K. Weiterentwicklung und Anwendung von quantenchemischen Methoden zur Berechnung von Molekülen im Magnetfeld. Dissertation, Karlsruhe Institute of Technology (KIT), Germany, 2018.

(158) Van Wüllen, C. Relativistic all-electron density functional calculations. *J. Comput. Chem.* **1999**, *20*, 51–62.

(159) OpenMP Architecture Review Boards, OpenMP API shared-memory parallel programming. `https://www.openmp.org` (retrieved December 4, 2020).

(160) Holzer, C.; Franzke, Y. J. OpenMP version of ridft, rdgrad, and egrad with contributions to mpshift, dscf, and grad; improved OpenMP version of aoforce and escf, released with TURBOMOLE V7.4 and further improved in TURBOMOLE V7.5.

(161) Belanzoni, P.; van Lenthe, E.; Baerends, E. J. An evaluation of the density functional approach in the zero order regular approximation for relativistic effects: Magnetic interactions in small metal compounds. *J. Chem. Phys.* **2001**, *114*, 4421–4433.

(162) Perdew, J. P. Density-functional approximation for the correlation energy of the inhomogeneous electron gas. *Phys. Rev. B* **1986**, *33*, 8822–8824.

(163) Becke, A. D. Density-functional exchange-energy approximation with correct asymptotic behavior. *Phys. Rev. A* **1988**, *38*, 3098–3100.

(164) Franzke, Y. J.; Spiske, L.; Pollak, P.; Weigend, F. Segmented Contracted Error-Consistent Basis Sets of Quadruple-ζ Valence Quality for One- and Two-Component Relativistic All-Electron Calculations. *J. Chem. Theory Comput.* **2020**, *16*, 5658–5674.

(165) Dyall, K. G. Relativistic Quadruple-Zeta and Revised Triple-Zeta and Double-Zeta Basis Sets for the 4p, 5p, and 6p Elements. *Theor. Chem. Acc.* **2006**, *115*, 441–447.

(166) Dyall, K. G. Relativistic double-zeta, triple-zeta, and quadruple-zeta basis sets for the actinides Ac–Lr. *Theor. Chem. Acc.* **2007**, *117*, 491–500.

(167) Gomes, A. S. P.; Dyall, K. G.; Visscher, L. Relativistic double-zeta, triple-zeta, and quadruple-zeta basis sets for the lanthanides La–Lu. *Theor. Chem. Acc.* **2010**, *127*, 369–381.

(168) Basis sets available from the Dirac program web site, `http://dirac.chem.sdu.dk` (retrieved December 4, 2020).

(169) Jensen, F. Basis Set Convergence of Nuclear Magnetic Shielding Constants Calculated by Density Functional Methods. *J. Chem. Theory Comput.* **2008**, *4*, 719–727.

(170) Jensen, F. Segmented Contracted Basis Sets Optimized for Nuclear Magnetic Shielding. *J. Chem. Theory Comput.* **2015**, *11*, 132–138.

(171) Perdew, J. P.; Burke, K.; Ernzerhof, M. Generalized Gradient Approximation Made Simple. *Phys. Rev. Lett.* **1996**, *77*, 3865–3868.

(172) Adamo, C.; Barone, V. Toward reliable density functional methods without adjustable parameters: The PBE0 model. *J. Chem. Phys.* **1999**, *110*, 6158–6170.

(173) Chai, J.-D.; Head-Gordon, M. Long-range corrected hybrid density functionals with damped atom–atom dispersion corrections. *Phys. Chem. Chem. Phys.* **2008**, *10*, 6615–6620.

(174) Treutler, O.; Ahlrichs, R. Efficient molecular numerical integration schemes. *J. Chem. Phys.* **1995**, *102*, 346–354.

(175) Treutler, O. Entwicklung und Anwendung von Dichtefunktionalmethoden. Ph.D. thesis, University of Karlsruhe (TH), Germany, 1995.

(176) Franzke, Y. J.; Treß, R.; Pazdera, T. M.; Weigend, F. Error-consistent segmented contracted all-electron relativistic basis sets of double- and triple-zeta quality for NMR shielding constants. *Phys. Chem. Chem. Phys.* **2019**, *21*, 16658–16664.

(177) Kutzelnigg, W.; Fleischer, U.; Schindler, M. The IGLO-Method: Ab-initio Calculation and Interpretation of NMR Chemical Shifts and Magnetic Susceptibilities. In *Deuterium and Shift Calculation*; Springer: Berlin, Heidelberg, Germany, 1991; pp 165–262.

(178) Noro, T.; Sekiya, M.; Koga, T. Segmented contracted basis sets for atoms H through Xe: Sapporo-(DK)-nZP sets (n = D, T, Q). *Theor. Chem. Acc.* **2012**, *131*, 1124.

(179) Noro, T.; Sekiya, M.; Koga, T. Sapporo-(DKH3)-nZP (n = D, T, Q) sets for the sixth period s-, d-, and p-block atoms. *Theor. Chem. Acc.* **2013**, *132*, 1363.

(180) Dunning, T. H. Gaussian basis sets for use in correlated molecular calculations. I. The atoms boron through neon and hydrogen. *J. Chem. Phys.* **1989**, *90*, 1007–1023.

(181) Woon, D. E.; Dunning, T. H. Gaussian basis sets for use in correlated molecular calculations. III. The atoms aluminum through argon. *J. Chem. Phys.* **1993**, *98*, 1358–1371.

(182) Jorge, F. E.; Canal Neto, A.; Camiletti, G. G.; Machado, S. F. Contracted Gaussian basis sets for Douglas–Kroll–Hess calculations: Estimating scalar relativistic effects of some atomic and molecular properties. *J. Chem. Phys.* **2009**, *130*, 064108.

(183) Campos, C. T.; Jorge, F. E. Triple zeta quality basis sets for atoms Rb through Xe: application in CCSD(T) atomic and molecular property calculations. *Mol. Phys.* **2013**, *111*, 167–173.

(184) Martins, L.; Jorge, F.; Machado, S. All-electron segmented contraction basis sets of triple zeta valence quality for the fifth-row elements. *Mol. Phys.* **2015**, *113*, 3578–3586.

(185) Zobel, J. P.; Widmark, P.-O.; Veryazov, V. The ANO-R Basis Set. *J. Chem. Theory Comput.* **2020**, *16*, 278–294.

(186) Roos, B. O.; Lindh, R.; Malmqvist, P.-Å.; Veryazov, V.; Widmark, P.-O. Main Group Atoms and Dimers Studied with a New Relativistic ANO Basis Set. *J. Phys. Chem. A* **2004**, *108*, 2851–2858.

(187) Roos, B. O.; Lindh, R.; Malmqvist, P.-Å.; Veryazov, V.; Widmark, P.-O. New Relativistic ANO Basis Sets for Transition Metal Atoms. *J. Phys. Chem. A* **2005**, *109*, 6575–6579.

(188) Dirac, P. A. M. Quantum Mechanics of Many-Electron Systems. *Proc. Roy. Soc. Lond. A* **1929**, *123*, 714–733.

(189) Slater, J. C. A Simplification of the Hartree-Fock Method. *Phys. Rev.* **1951**, *81*, 385–390.

(190) Vosko, S. H.; Wilk, L.; Nusair, M. Accurate spin-dependent electron liquid correlation energies for local spin density calculations: a critical analysis. *Can. J. Phys.* **1980**, *58*, 1200–1211.

(191) Keal, T. W.; Tozer, D. J. A semiempirical generalized gradient approximation exchange-correlation functional. *J. Chem. Phys.* **2004**, *121*, 5654–5660.

(192) Tao, J.; Perdew, J. P.; Staroverov, V. N.; Scuseria, G. E. Climbing the Density Functional Ladder: Nonempirical Meta–Generalized Gradient Approximation Designed for Molecules and Solids. *Phys. Rev. Lett.* **2003**, *91*, 146401.

(193) Perdew, J. P.; Ruzsinszky, A.; Csonka, G. I.; Constantin, L. A.; Sun, J. Workhorse Semilocal Density Functional for Condensed Matter Physics and Quantum Chemistry. *Phys. Rev. Lett.* **2009**, *103*, 026403.

(194) Perdew, J. P.; Ruzsinszky, A.; Csonka, G. I.; Constantin, L. A.; Sun, J. Erratum: Workhorse Semilocal Density Functional for Condensed Matter Physics and Quantum Chemistry [Phys. Rev. Lett. 103, 026403 (2009)]. *Phys. Rev. Lett.* **2011**, *106*, 179902.

(195) Furness, J. W.; Kaplan, A. D.; Ning, J.; Perdew, J. P.; Sun, J. Accurate and Numerically Efficient r^{2}SCAN Meta-Generalized Gradient Approximation. *J. Chem. Phys. Lett.* **2020**, *11*, 8208–8215.

(196) Furness, J. W.; Kaplan, A. D.; Ning, J.; Perdew, J. P.; Sun, J. Correction to "Accurate and Numerically Efficient r²SCAN Meta-Generalized Gradient Approximation". *J. Phys. Chem. Lett.* **2020**, *11*, 9248–9248.

(197) Lee, C.; Yang, W.; Parr, R. G. Development of the Colle-Salvetti correlation-energy formula into a functional of the electron density. *Phys. Rev. B* **1988**, *37*, 785–789.

(198) Becke, A. D. A new mixing of Hartree–Fock and local density-functional theories. *J. Chem. Phys.* **1993**, *98*, 1372–1377.

(199) Becke, A. D. Density-functional thermochemistry. III. The role of exact exchange. *J. Chem. Phys.* **1993**, *98*, 5648–5652.

(200) Becke, A. D. Density-functional thermochemistry. V. Systematic optimization of exchange-correlation functionals. *J. Phys. Chem.* **1997**, *107*, 8554–8560.

(201) Wilson, P. J.; Bradley, T. J.; Tozer, D. J. Hybrid exchange-correlation functional determined from thermochemical data and ab initio potentials. *J. Chem. Phys.* **2001**, *115*, 9233–9242.

(202) Staroverov, V. N.; Scuseria, G. E.; Tao, J.; Perdew, J. P. Comparative assessment of a new nonempirical density functional: Molecules and hydrogen-bonded complexes. *J. Chem. Phys.* **2003**, *119*, 12129–12137.

(203) Grimme, S. Accurate Calculation of the Heats of Formation for Large Main Group Compounds with Spin-Component Scaled MP2 Methods. *J. Phys. Chem. A* **2005**, *109*, 3067–3077.

(204) Yanai, T.; Tew, D. P.; Handy, N. C. A new hybrid exchange–correlation functional using the Coulomb-attenuating method (CAM-B3LYP). *Chem. Phys. Lett.* **2004**, *393*, 51–57.

(205) Jin, Y.; Bartlett, R. J. The QTP family of consistent functionals and potentials in Kohn-Sham density functional theory. *J. Chem. Phys.* **2016**, *145*, 034107.

(206) Haiduke, R. L. A.; Bartlett, R. J. Communication: Can excitation energies be obtained from orbital energies in a correlated orbital theory? *J. Chem. Phys.* **2018**, *149*, 131101.

(207) Heyd, J.; Scuseria, G. E.; Ernzerhof, M. Hybrid functionals based on a screened Coulomb potential. *J. Chem. Phys.* **2003**, *118*, 8207–8215.

(208) Heyd, J.; Scuseria, G. E.; Ernzerhof, M. Erratum: "Hybrid functionals based on a screened Coulomb potential" [J. Chem. Phys. 118, 8207 (2003)]. *J. Phys. Chem.* **2006**, *124*, 219906.

(209) Krukau, A. V.; Vydrov, O. A.; Izmaylov, A. F.; Scuseria, G. E. Influence of the exchange screening parameter on the performance of screened hybrid functionals. *J. Phys. Chem.* **2006**, *125*, 224106.

(210) Vydrov, O. A.; Scuseria, G. E. Assessment of a long-range corrected hybrid functional. *J. Chem. Phys.* **2006**, *125*, 234109.

(211) Schmitte, J.; Friebel, C.; Weller, F.; Dehnicke, K. Synthese, IR- und EPR-Spektren sowie die Kristallstruktur von $(PPh_3Me)_2[MoNCl_4]$. *Z. Anorg. Allg. Chem.* **1982**, *495*, 148–156.

(212) Sunil, K. K.; Rogers, M. T. ESR studies of some oxotetrahalo complexes of vanadium(IV) and molybdenum(V). *Inorg. Chem.* **1981**, *20*, 3283–3287.

(213) Manoharan, P. T.; Rogers, M. T. Ligand Hyperfine Interactions in Molybdenyl and Chromyl Halide Complexes. *J. Chem. Phys.* **1968**, *49*, 5510–5519.

(214) van Kemenade, J. T. C. Ligand Hyperfine Interactions in Oxyhalides of Pentavalent Chromium, Molybdenum and Tungsten. Ph.D. thesis, Technical University Delft, The Netherlands, 1970.

(215) Baldas, J.; Boas, J. F.; Bonnyman, J. Preparation and Properties of Nitridotechnetic (VI) Acid. I. Observation of the ESR-Spectrum of the [TcNF$_4$]$^-$ Anion in Hydrofluoric Acid Solution. *Aus. J. Chem.* **1989**, *42*, 639–648.

(216) Baldas, J.; Boas, J. F.; Bonnyman, J.; Williams, G. A. Studies of technetium complexes. Part 6. The preparation, characterisation, and electron spin resonance spectra of salts of tetrachloro- and tetrabromo-nitridotechnetate(VI): crystal structure of tetraphenylarsonium tetrachloronitridotechnetate(VI). *J. Chem. Soc., Dalton Trans.* **1984**, 2395–2400.

(217) Kersting, M.; Friebel, C.; Dehnicke, K.; Krestel, M.; Allmann, R. Synthese, IR- und EPR-Spektren sowie die Kristallstruktur von HPPh$_3$[WOCl$_4$(OPPh$_3$)]. *Z. Anorg. Allg. Chem.* **1988**, *563*, 70–78.

(218) Voigt, A.; Abram, U.; Kirmse, R. The existence of [ReNF$_4$]$^-$ – an EPR study. *Inorg. Chem. Commun.* **1998**, *1*, 141–142.

(219) Voigt, A.; Abram, U.; Böttcher, R.; Richter, U.; Reinhold, J.; Kirmse, R. Q-Band single-crystal EPR study and molecular orbital calculations of [(C$_6$H$_5$)$_4$As][Re^{VI}NCl$_4$/Re^{V}OCl$_4$]. *Chem. Phys.* **2000**, *253*, 171–181.

(220) Abram, U.; Braun, M.; Abram, S.; Kirmse, R.; Voigt, A. [NBu$_4$][ReNCl$_4$]: Facile synthesis, structure, electron paramagnetic resonance spectroscopy and reactions. *J. Chem. Soc., Dalton Trans.* **1998**, 231–238.

(221) Borisova, L. V.; Ermakov, A. N.; Plastinina, Y. I.; Prasolova, O. D.; Marov, I. N. Determination of rhenium based on the formation of rhenium(VI) oxide halide complexes by spectrophotometry and electron spin resonance spectroscopy. *Analyst* **1982**, *107*, 500–504.

(222) Holloway, J. H.; Hope, E. G.; Raynor, J. B.; Townson, P. T. Magnetic resonance studies on osmium pentafluoride oxide. *J. Chem. Soc., Dalton Trans.* **1992**, 1131–1134.

(223) Manual of TURBOMOLE V7.5.1 2021, a development of University of Karlsruhe and Forschungszentrum Karlsruhe GmbH, 1989-2007, TURBOMOLE GmbH, since 2007; available from `https://www.turbomole.org/turbomole/turbomole-documentation/` (retrieved August 28, 2021).

(224) Dyall, K. G. Relativistic double-zeta, triple-zeta, and quadruple-zeta basis sets for the 6d elements Rf–Cn. *Theor. Chem. Acc.* **2011**, *129*, 603–613.

(225) Luber, S.; Malkin Ondík, I.; Reiher, M. Electromagnetic fields in relativistic one-particle equations. *Chem. Phys.* **2009**, *356*, 205–218.

(226) Weltner Jr., W. *Magnetic Atoms and Molecules*; Van Nostrand Reinhold: New York, USA, 1983.

(227) Holzer, C.; Franzke, Y. J.; Kehry, M. Assessing the Accuracy of Local Hybrid Density Functional Approximations for Molecular Response Properties. *J. Chem. Theory Comput.* **2021**, *17*, 2928–2947.

(228) Lehtola, S.; Dimitrova, M.; Fliegl, H.; Sundholm, D. Benchmarking Magnetizabilities with Recent Density Functionals. *J. Chem. Theory Comput.* **2021**, *17*, 1457–1468.

(229) Lehtola, S.; Dimitrova, M.; Fliegl, H.; Sundholm, D. Correction to "Benchmarking Magnetizabilities with Recent Density Functionals". *J. Chem. Theory Comput.* **2021**, *17*, 1457–1468.

(230) Teale, A. M.; Lutnæs, O. B.; Helgaker, T.; Tozer, D. J.; Gauss, J. Benchmarking density-functional theory calculations of NMR shielding constants and spin–rotation constants using accurate coupled-cluster calculations. *J. Chem. Phys.* **2013**, *138*, 024111.

(231) Hedegård, E. D.; Kongsted, J.; Sauer, S. P. A. Validating and Analyzing EPR Hyper-

fine Coupling Constants with Density Functional Theory. *J. Chem. Theory Comput.* **2013**, *9*, 2380–2388.

(232) Flaig, D.; Maurer, M.; Hanni, M.; Braunger, K.; Kick, L.; Thubauville, M.; Ochsenfeld, C. Benchmarking Hydrogen and Carbon NMR Chemical Shifts at HF, DFT, and MP2 Levels. *J. Chem. Theory Comput.* **2014**, *10*, 572–578.

(233) Stoychev, G. L.; Auer, A. A.; Izsák, R.; Neese, F. Self-Consistent Field Calculation of Nuclear Magnetic Resonance Chemical Shielding Constants Using Gauge-Including Atomic Orbitals and Approximate Two-Electron Integrals. *J. Chem. Theory Comput.* **2018**, *14*, 619–637.

(234) Lutnæs, O. B.; Teale, A. M.; Helgaker, T.; Tozer, D. J.; Ruud, K.; Gauss, J. Benchmarking density-functional-theory calculations of rotational g tensors and magnetizabilities using accurate coupled-cluster calculations. *J. Chem. Phys.* **2009**, *131*, 144104.

(235) Alonso, P.; Alcalá, R.; Usón, R.; Forniés, J. EPR study of mononuclear Pt(III) organometallic complexes. *J. Phys. Chem. Solids* **1991**, *52*, 975–978.

(236) Komorovský, S.; Repiský, M.; Ruud, K.; Malkina, O. L.; Malkin, V. G. Four-Component Relativistic Density Functional Theory Calculations of NMR Shielding Tensors for Paramagnetic Systems. *J. Phys. Chem. A* **2013**, *117*, 14209–14219.

(237) Ramsey, N. F. Magnetic Shielding of Nuclei in Molecules. *Phys. Rev.* **1950**, *78*, 699–703.

(238) Ramsey, N. F. Dependence of Magnetic Shielding of Nuclei upon Molecular Orientation. *Phys. Rev.* **1951**, *83*, 540–541.